The Astrophysical Journal, 868:105 (19pp), 2018 December 1 https://doi.org/10.3847/1538-4357/aae712

Tracing the Origin of Moving Groups. II. Chemical Abundance of Six Stars in the Halo Stream LAMOST-N1

J. K. Zhao[1], G. Zhao[1,2], W. Aoki[3,4], M. N. Ishigaki[5], T. Suda[6], T. Matsuno[3,4], J. R. Shi[1], Q. F. Xing[1], Y. Q. Chen[1,2], Terry D. Oswalt[7], X. M. Kong[1,2], and X. L. Liang[1,2]

[1] Key Laboratory of Optical Astronomy, National Astronomical Observatories, Chinese Academy of Sciences, Beijing 100012, People's Republic of China; zjk@nao.cas.cn, gzhao@nao.cas.cn
[2] School of Astronomy and Space Science, University of Chinese Academy of Sciences, Beijing 100049, People's Republic of China
[3] National Astronomical Observatory of Japan, 2-21-1 Osawa, Mitaka, Tokyo 181-8588, Japan
[4] Department of Astronomical Science, School of Physical Sciences, The Graduate University of Advanced Studies (SOKENDAI), 2-21-1 Osawa, Mitaka, Tokyo 181-8588, Japan; aoki.wako@nao.ac.jp
[5] Kavli Institute for the Physics and Mathematics of the Universe (WPI), Todai Institute for Advanced Study, University of Tokyo, 5-1-5 Kashiwanoha, Kashiwa, 277-8583 Chiba, Japan; miho.ishigaki@ipmu.jp
[6] Research Center for the Early Universe, The University of Tokyo, 7-3-1 Hongo, Bunkyo-ku, Tokyo 113-0033, Japan
[7] Embry-Riddle Aeronautical University, 600 S. Clyde Morris Boulevard, Daytona Beach, FL 32114, USA; oswaltt1@erau.edu
Received 2018 July 23; revised 2018 September 30; accepted 2018 October 7; published 2018 November 27

Abstract

We present the chemical abundances of six stars in the halo stream Large Sky Area Multi-Object Fiber Spectroscopic Telescope (LAMOST)-N1, a new kinematically selected substructure from LAMOST data, from high-resolution spectra obtained with the Subaru/High Dispersion Spectrograph. Atmospheric parameters were determined by an iterative procedure based on spectroscopic analysis. Abundances of 11 elements, including α elements (Mg, Ca, Ti), odd-Z light elements (Na), iron-peak elements (Sc, Cr, Mn, Fe, Ni), and neutron-capture elements (Y, Ba), are measured by local thermodynamic equilibrium analysis procedures. [Fe/H] of the six stars ranges from -1.5 to -0.66. The abundance patterns of α elements show a similar trend to those of low-α stars in Nissen et al. and over 0.1 dex lower than those of Galactic field stars. The Sc, Cr, Mn, and Ni abundances of these six stars exhibit a positive trend with increasing iron abundance, with varying gradients. In addition, abundance distribution between [Na/Fe] and [Ni/Fe] and between that of [Ba/Y] and [Fe/H] of these six stars is different from both Galactic stars and the known dwarf galaxies. Our results suggest that LAMOST-N1 might be a relic of a system with slower chemical evolutions than the Milky Way.

Key words: Galaxy: kinematics and dynamics – stars: abundances – stars: late-type

1. Introduction

Stellar streams are purported to be remnants of the hierarchical merger process predicted by the Lambda cold dark matter (ΛCDM) theory. They were first detected in the Milky Way and other galaxies in the Local Group and have been detected in much more distant galaxies (Martínez-Delgado et al. 2015). The stellar streams could be tidal debris of a dwarf galaxy or a star cluster accreted from external systems. Alternatively, a stream can be associated with a dynamical interaction between the Galactic disk and an accreting dwarf galaxy. Understanding the origins of individual stellar streams, therefore, is important to examine the hierarchical merging and interaction history of the Milky Way in great detail. Tidal debris of dwarf galaxies or globular clusters recently accreted by the Milky Way can be identified as spatially coherent streams. Optical matched filtering can be used to find overdensities in spatial position or color–magnitude locus using photometric data. The Sagittarius stream (Ibata et al. 1994; Majewski et al. 2003) is the most well-known stream of this type. Later, couples of spatially coherent streams such as GD-1 (Grillmair & Dionatos 2006), the Orphan stream (Belokurov et al. 2006), and Pal5 (Odenkirchen et al. 2001) have been identified. So far, more than 20 streams in this stage have been detected in digital sky surveys, such as the Two Micron All Sky Survey (2MASS; Skrutskie et al. 2006), the Sloan Digital Sky Survey (SDSS; York et al. 2000), Pan-STARRS1 (Chambers et al. 2016.), etc. Such spatially coherent streams can be dispersed in the configuration space as they interact with the gravitational potential of the Milky Way. In this case, streams can be identified as a clump in the phase space (i.e., energy, angular momentum, or eccentricity). H99 (Helmi et al. 1999) is a representative stream in this stage, which was detected in angular momentum phase space with a sample of metal-poor stars. Finally, member stars of a stream only have consistent chemical composition, but do not clump in spatial position and phase space. Instead, the chemical prints can be used to identified them. The α-poor stars (Xing & Zhao 2014) might belong to a stream in this stage.

The detection of streams that do not spatially coherent requires kinematic information: radial velocity and proper motion. Therefore, spectroscopy and astrometry are indispensable. Helmi et al. (1999) discovered a stream that occupied the same region in the (L_z, $L_\perp$) plane with a sample composed of metal-poor stars. Later, this stream was confirmed by Chiba & Beers (2000) with a different data set. Helmi et al. (2006) searched for signatures of past accretion events in the Milky Way with a catalog by Nordström et al. (2004), which contains accurate spatial and kinematic information as well as metallicities for 13,240 nearby stars. They found a wealth of substructure in APL space (the apocenter (A) and pericenter (P), as well as their z-angular momentum (L_Z)). Dettbarn et al. (2007) analyzed the phase-space distribution in a sample of non-kinematically selected low-metallicity stars in the solar vicinity and determined the orbital parameters of several halo streams. One of those streams seemed to have precisely the same kinematics as the Sagittarius stream. Klement et al. (2008) searched for stellar streams or moving groups in the solar neighborhood in (V, $\sqrt{U^2 + 2V^2}$) space, using data provided by the Radial Velocity Experiment (RAVE; Steinmetz et al. 2006) public data release. They estimated

overdensities related to the Sirius, Hercules, Arcturus, and Hyades-Pleiades moving groups. Also, they found a new stream candidate (K08), suggesting that its origin was external to the Milky Ways disk. With the SDSS Data Release 7, Klement et al. (2009) identified at least five significant phase-space overdensities of stars on very similar orbits in the solar neighborhood. At least two are new genuine halo streams, judged by their kinematics and [Fe/H], respectively. Zhao et al. (2014) analyzed the kinematics of thick-disk and halo stars from Large Sky Area Multi-Object Fiber Spectroscopic Telescope (LAMOST; Cui et al. 2012; Zhao et al. 2012) DR1 and found evidence for a new stream designated V3 (centered at $V \sim -180\,\mathrm{km\,s^{-1}}$) in the halo. With LAMOST DR2, six stream candidates were detected by Zhao et al. (2015).

The chemical composition of individual member stars helps in understanding the formation and evolution of stellar streams. For some of the known streams, however, their origins remain controversial. For example, the H99 stream (Helmi et al. 1999) was deemed to be a relic of a satellite with simulations. Roederer et al. (2010) obtained high-resolution and high signal-to-noise ratio (S/N) spectra of 12 probable stream members of H99 and derived abundances or upper limits for 51 species of 46 elements in each of the stars. The stream members show a range of metallicity ($-3.4 < [\mathrm{Fe/H}] < -1.5$), but are otherwise chemically homogeneous. They have the same star-to-star dispersion in [X/Fe] as the rest of the halo, which does not support an extragalactic origin. For the Kapteyn group, Navarrete et al. (2015) analyzed the optical and near-infrared high-resolution, high S/N spectroscopic study of 14 stars of the Kapteyn group, plus 10 additional stars (the *ωCen* group). The resulting Na-O and Mg-Al patterns for stars of the combined Kapteyn and *ωCen* group samples do not resemble those of the globular cluster *ωCen*, and are not different from those of field stars of the Galactic halo. Thus, they concluded that the Kapteyn stream is not tidal debris from *ωCen*, at variance with Wylie-de Boer et al. (2010). K08 was considered to be a part of the tidal debris from an accreted satellite by Klement et al. (2008). However, Liu et al. (2015) did a detailed abundance analysis of 16 stream stars and suggested that this stream originated from the thick-disc population, which was perturbed by a massive merger in the early universe.

The LAMOST-Subaru joint observation program provided opportunities to observe some member stars of halo streams detected with LAMOST (Zhao et al. 2015). Our goal is to confirm the existence of the stream and examine whether they are the debris from a dSph (or a globular cluster) or just a dynamical group. In Liang et al. (2018, hereafter paper I), we investigated the origin of the γ Leo moving group. In this paper, we present our study of six stars in the halo stream LAMOST-N1 (Zhao et al. 2015).

In Section 2, we describe the observations and data reduction. Section 3 discusses in detail our abundance determinations. Our results and discussion are illustrated in Section 4. Finally, our main conclusions and suggestions are summarized in Section 5.

2. Observation and Data Reduction

2.1. Sample Selection

The sample stars are selected from candidate member stars of the stream LAMOST-N1 (Zhao et al. 2015). LAMOST-N1 has been identified as a clump in the phase space of (ν, V_{az}, $V_{\Delta E}$) space, where ν is the angle between the orbital plane (which is fixed in a spherical potential) and the direction toward the north galactic pole and ranges from 0° to 180°. V_{az} is related to the angular momentum and $V_{\Delta E}$ is a measure of a stars eccentricity. The candidate member stars are selected in the following manner: V_{az} ranges in [50, 100] $\mathrm{km\,s^{-1}}$ and $V_{\Delta E}$ ranges in [150, 210] $\mathrm{km\,s^{-1}}$; ν ranges in [15°, 25°], which is a peak in the ν distribution; and a value of the wavelet transformation in N1 of at least 90% of its maximum value. About 35 member star candidates meet the above criteria. Figure 1 shows the Toomre diagram for stars in Zhao et al. (2015). The member stars are marked with diamonds. The dotted line is the division line of stars with prograde orbit and retrograde orbit. Obviously, member stars are with halo-like kinematics and prograde motion.

2.2. Subaru/High Dispersion Spectrograph Observations

Eight brighter stars are selected from the 35 candidates with $r <$ 14.7 and are available for observation during the two observing runs in 2016 November and 2017 February with the Subaru/High Dispersion Spectrograph (HDS) as part of the LAMOST-Subaru joint program. For these eight candidate members, snapshot high-resolution spectra are acquired with a resolving power of $R \sim 36{,}000$ and exposure times of 10–80 minutes. Among the eight stars, two were found to be double-lined spectroscopic binaries and were excluded. Data reductions are carried out using the IRAF echelle package including bias-level correction, scattered light subtraction, flat-fielding, extraction of spectra, and wavelength calibration using Th arc lines. Cosmic-ray hits are removed by the method described in Aoki et al. (2005). Radial velocities (RV) of the stars are obtained using the code HDSV (Zhao et al. 2007) by correlation between the observed spectra with solar atlas. The uncertainties of the RV is smaller than 1.0 $\mathrm{km\,s^{-1}}$. The continuum is determined by fitting several windows with a low-order polynomial. Table 1 provides the observational information for the remaining six stars. Besides our program stars, five comparison stars (G18-24, G188-22, HD 193901, HD 196892, and HD 111980) are selected from Ishigaki et al. (2012) to examine the consistency between the present work and previous ones.

2.3. Equivalent Width Measurement

The equivalent widths (EWs) are measured in normalized spectra. For weak lines, the line profiles are usually well reproduced by a Gaussian function, and direct integration is applied for strong lines (EW > 120 mÅ). For most of the elements, we choose lines with EW between 10 and 120 mÅ. For some other elements (e.g., Na, Ba), we opt to use lines with EWs stronger than 120 mÅ due to the availability of few lines throughout the spectra. Table 3 lists the available EWs of each species for these six stars.

We compares EWs determined by the above procedure with those of Ishigaki et al. (2012) using comparison stars to examine the consistency between the two works. In Ishigaki et al. (2012), the EWs are measured with a Gaussian fitting. Figure 2 shows the EW comparison for HD 111980. The *x*-axis shows the EWs from Ishigaki et al. (2012) while the *y*-axis represents our measurements. The standard deviation is about 0.8 mÅ for this star and the max standard deviation among

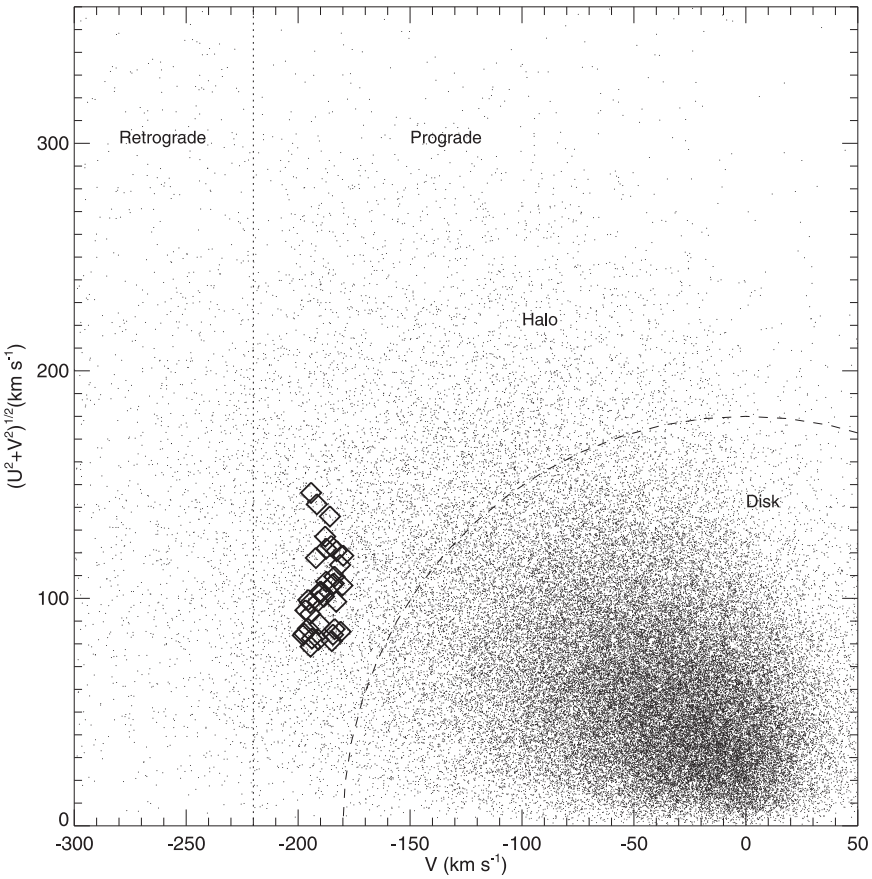

Figure 1. Toomre diagram for stars in Zhao et al. (2015). Diamonds represent the 35 member candidates in LAMOST-N1. The long-dashed line corresponds to Vtotal = 180 km s^{-1}. The short-dashed line indicates zero rotation in the Galaxy.

Table 1
Basic Parameters of the Six Stars and the Subaru/HDS Observation

ID	R.A. (degree)	Decl. (degree)	r_0	S/N[a]	Date	RV (km s^{-1})	eRV (km s^{-1})
J0054+3047	13.503481	30.797329	14.2261	40	2016 Nov 18	−169.05	0.19
J0147+2742	26.861045	27.705449	14.4878	35	2016 Nov 18	−198.85	0.41
J2158+2840	329.585999	28.675182	13.9799	38	2016 Nov 18	−196.05	0.29
J2350+2622	357.5523	26.37558	14.6732	34	2016 Nov 18	−174.64	0.17
J1218+2852	184.632775	28.868973	13.9921	52	2017 Feb 16	85.8	0.14
J1046+5004	161.522975	50.067471	14.5725	45	2017 Feb 16	65.08	0.27

Note.
[a] S/N per pixel was measured at $\lambda \sim 5170$ Å.

these five comparison stars is less than 1 mÅ, indicating that both of the measurements are very consistent.

3. Abundance Determination

Chemical abundances are determined by a standard analysis for measured EWs with the ATLAS NEWODF grid of model atmospheres, assuming no convective overshooting (Castelli & Kurucz 2003). We adopt the photospheric solar abundances of Asplund et al. (2009) when calculating the [X/H] and [X/Fe] abundance ratios.

3.1. Determination of the Atmospheric Parameters

To calculate elemental abundance, stellar parameters need to be determined first. At the beginning, the effective temperature ($T_{\rm eff}$) is estimated using two empirical calibrations. One is based on the photometric color index $(g-k2)0$ and the empirical calibration relations by Huang et al. (2015). The other is estimated from the $(V-K)_0$ using the temperature scales of Casagrande et al. (2010). The g magnitudes are from SDSS and the $k2$ and K magnitudes are from 2MASS. V magnitudes in the Johnson V system are taken from SIMBAD. Next, the $T_{\rm eff}$ from the $(g-k2)_0$ is set to an initial value. The initial values of surface gravity (log g) and metallicity ([Fe/H]) are from the LAMOST pipeline (Luo et al. 2015) and 1.5 km s^{-1} is adopted as the initial microturbulence (ξ_t). The ultimate $T_{\rm eff}$ is determined by the excitation equilibrium method, which requires no trend of abundances from Fe I lines against excitation potentials. We estimate the final value of log g by forcing the Fe I and Fe II lines to yield almost the same

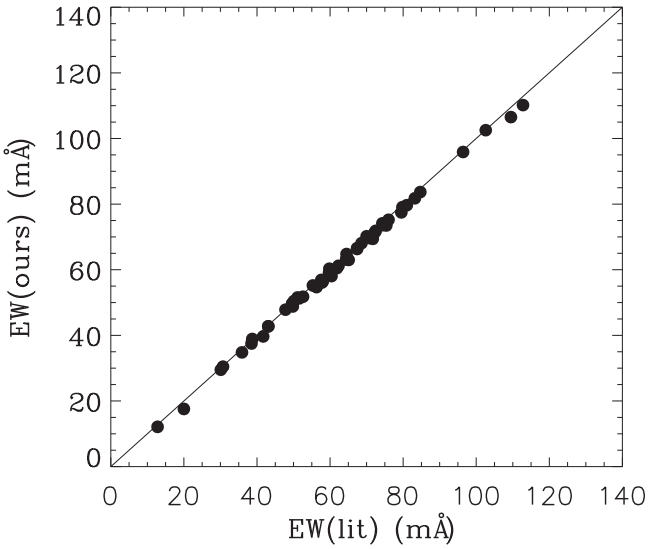

Figure 2. EW comparison for HD 111908 between our results and those in Ishigaki et al. (2012). The solid line indicates the unit slope.

iron abundance. The ξ_t was determined by forcing the iron abundance from different Fe I lines until they show no dependence on their EWs. The final results were adopted by iterating the whole processes until they were consistent. For log g values, the Fe ionization equilibrium method is known to yield biased estimates if Fe I Lines are not formed in local thermal equilibrium (LTE; Bergemann et al. 2012). Sitnova et al. (2015) studied the non-LTE (NLTE) effect on F and G dwarfs and they suggested that the shift in log g is smaller than 0.1 dex for stars with [Fe/H] > -0.75, $T_{\rm eff} < 5750$ or log > 4.20. Moreover, from the Figure 4 in Lind et al. (2012), we estimated that the NLTE effect on log g derived from the ionization balance of our stars is smaller than 0.1 dex for our six program stars.

Figure 3 compares $T_{\rm eff}$ derived from the photometric color index, the LAMOST pipeline, and the excitation potential equilibrium. $T_{\rm eff}$_HY is derived from $(g-k2)_0$ based on the empirical calibration by Huang et al. (2015), $T_{\rm eff}$_casa is derived from $(V-K)_0$ based on the empirical calibration by Casagrande et al. (2010), $T_{\rm eff}$_lasp is provided by the LAMOST pipeline, and $T_{\rm eff}$_spa is our adopted value from the equilibrium method. The top panel of Figure 3 shows the comparison of $T_{\rm eff}$ between the values $T_{\rm eff}$_HY and $T_{\rm eff}$_lasp. The systematic offset is about 23 K and the scatter is 96 K, which indicates that the LAMOST pipeline provides consistent $T_{\rm eff}$ with those from the photometric color index although the left three points show relatively large scatter. The middle panel of Figure 3 compares $T_{\rm eff}$_HY and $T_{\rm eff}$_casa. There is a ~160 K systematic offset between these these two values, but the scatter is very small. The bottom panel compares $T_{\rm eff}$_HY and $T_{\rm eff}$_spa. It is evident that these two values are very consistent. Table 2 lists the stellar parameters of these six stars from the LAMOST pipeline and the values from the equilibrium method. In general, the agreement between the two values is fairly good. Among the three parameters, log g shows larger differences, reflecting the situation that log g is not as sensitive to the spectral profile as $T_{\rm eff}$ and [Fe/H].

3.2. Elemental Abundance

The atomic lines selected for this research are covered by the spectrum of 4370 ~ 6770 Å. The detailed information on these is drawn mainly from Aoki et al. (2013) and Li et al. (2015), listed in Table 3. Except for Y, we calculate the element abundances with the ABONTEST8 program supplied by P. Magain (2018, private communication), based on the homogeneous, plane-parallel, and local thermodynamic equilibrium models of Castelli & Kurucz (2003). The program matches the observed EWs with theoretical values based on atmospheric models. The calculation takes into account natural broadening, van derWaals damping broadening, and thermal broadening. Since only one line of Y is available in our line list, the Y abundance is derived using spectrum fitting with Y II 4398.013 Å. Figure 4 shows an example of the Y abundance determination for the star J1218+2852. The black open circles represent the observed spectra. A grid of theoretical spectra with different Y abundances are then computed. The final Y abundance is adopted by the corresponding theoretical spectrum with the least χ^2 between the observed and theoretical spectra. The blue dotted line in the Figure 4 is the best matching theoretical spectrum. Because of the limited S/N around the Y II line in J0147+2742, [Y/Fe] is not measured in this star.

We derive the [X/Fe] ratios of 10 elements (Na, Mg, Ca, Sc, Ti, Cr, Mn, Ni, Ba, and Y). The abundances were determined using the measured EWs (Y with spectrum fitting) adopting the stellar parameters in Table 2. Seriously blended lines were not used because of the large uncertainty in the final abundance determination.

For all of the program stars, the abundances of these α elements (Mg, Ca, and Ti) have been determined. About 20 Ca I lines, 2–4 Mg I lines, 7–17 Ti I lines, and 15–16 Ti II lines have continuum levels that are well estimated. Regarding the light odd-Z elements, we measure the abundance of Na from four Na I lines. For star J0147+2742, only two NaD lines are used because other Na lines are too weak.

The abundances of Fe-peak elements (Sc, Cr, Mn, and Ni) are determined using 5–7 Sc II lines, 2–12 Cr I lines, 2–3 Mn I lines, and 7–14 Ni I lines. The abundance of Ba is determined from 4 to 5 Ba II lines. The Y II line at 4398 Å is used to derive the abundance by a spectral fitting as mentioned above. The number of selected lines for each star is influenced by the metallicity and S/N. Moreover, the lines are removed from which abundances deviated by more than 3σ from the average calculated for an atomic species from multiple lines. We did not consider the effect of the hyperfine splitting structure (HFS) of Sc II, Mn I, and Ba II. For our sample, five stars are with [Fe/H] < -1.0 and one star with [Fe/H] ~ -0.7. Based on the Figure 1 of McWilliam (1998), the HFS effect of Ba II is very small for stars with [Fe/H] < -0.8. Also, Ishigaki et al. (2013) suggested that the HFS effect of Sc II is very small at about 0.03 dex for their sample. The Mn abundance in our paper is not mainly used to determine the origin of LAMOST-N1. Thus, we neglected the HFS effects for Sc II, Mn I, and Ba II in the abundance determination.

The final stellar abundances in the [X/Fe] are presented in Table 4. Since the Ti abundance from Ti I lines is not reliable (Bergemann 2011), the [Ti/Fe] ratio for each star is adopted from the Ti II lines. We found no previous abundance

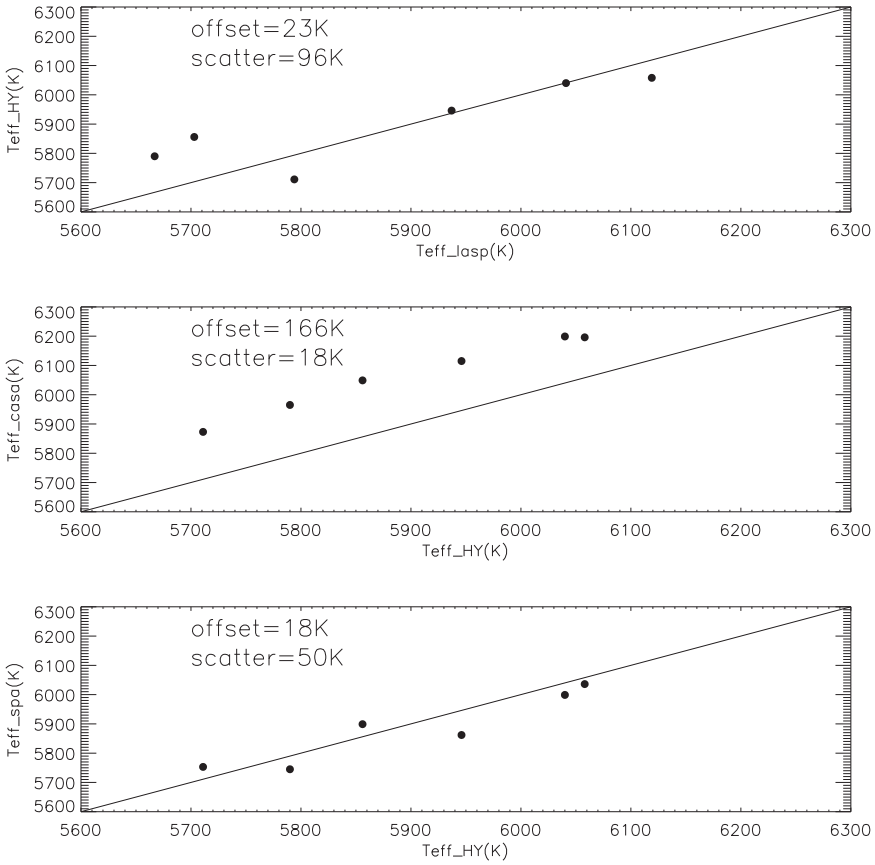

Figure 3. $T_{\rm eff}$ comparison from the photometric color index, LAMOST pipeline, and the excitation equilibrium. Top: $T_{\rm eff}$_hy vs. $T_{\rm eff}$_lasp. Middle: $T_{\rm eff}$_casa vs. $T_{\rm eff}$_hy. Bottom: $T_{\rm eff}$_spa vs. $T_{\rm eff}$_hy. The solid lines indicate the unit slope.

Table 2
Stellar Parameters of the Six Stars

ID	$T_{\rm eff}$_lasp (K)	log g_lasp	[Fe/H]_lasp	$T_{\rm eff}$_spa (K)	log g_spa	[Fe/H]_spa	ξ_t (km s^{-1})
J0054+3047	5794	4.286	−1.287	5753	4.80	−1.34	0.7
J0147+2742	5937	4.22	−1.417	5862	4.01	−1.48	1.3
J2158+2840	5667	4.23	−1.074	5745	4.73	−1.00	0.9
J2350+2622	6119	4.254	−0.938	6036	3.95	−1.14	1.9
J1218+2852	6041	4.15	−0.922	5999	4.15	−0.95	1.5
J1046+5004	5703	4.408	−0.783	5899	4.91	−0.66	1.0

measurements for any of the six stars in the present sample. To confirm the consistency of our abundance measurements with those of previous studies, we have conducted an abundance analysis for five comparison stars and provided them in Table 4 (see below).

3.3. Uncertainties

There are two dominant sources of uncertainty in the abundance measurements. One is the EW errors, which are explicitly propagated into our abundance estimates. The uncertainties in the stellar parameters ($T_{\rm eff}$, log g, [Fe/H], and ξ_t) are another source of error. We estimated the impact of each factor of the analysis by changing each quantity separately (leaving the others unchanged). Tables 5 and 6 list the abundance differences by changing the EW by 2 mÅ, the effective temperature by 100 K, the surface gravity by 0.15 dex, the iron abundance by 0.15 dex, and the microturbulent velocity by 0.2 km s^{-1}. Finally, we took the square root of the quadratic sum of the errors associated with all factors to calculate the total error. As seen in Tables 5 and 6, for most of the chemical elements, the uncertainties are less than 0.13 dex. The atomic data of lines are from Aoki et al. (2013) and Li et al. (2015), which are useful to measure the abundance. The error budget of most species can be negligible. Thus, the uncertainties of the log gf values have not been considered in the uncertainty estimation of the abundance derivations.

To examine the consistency between the present check to see if our abundance results in a systematic error, we also measure the abundance of five calibration stars following the same routine as the member stars, except that the stellar parameters are from Ishigaki et al. (2012). Figure 5 shows the [X/Fe] comparison between our results and those of Ishigaki et al. (2012). We confirm that the two measurements are consistent and no offset error exists in the two abundance calculations.

Table 3
Spectral Line Data and Equivalent Width

Wavelength (Å)	Species	L.E.P. (eV)	log *gf*	J0054 (mÅ)	J0147 (mÅ)	J2158 (mÅ)	J2350 (mÅ)	J1218 (mÅ)	J1046 (mÅ)
4314.095	Sc II	0.62	0.100	⋯	⋯	⋯	⋯	⋯	102.8
4318.652	Ca I	1.89	−0.207	⋯	⋯	⋯	⋯	⋯	88.8
4320.745	Sc II	0.60	−0.250	⋯	⋯	⋯	⋯	⋯	80.4
4369.771	Fe I	3.05	−0.800	⋯	⋯	⋯	⋯	⋯	80.1
4374.457	Sc II	0.62	−0.418	56.3	⋯	⋯	⋯	⋯	74.6
4375.930	Fe I	0.00	−3.020	100.2	⋯	⋯	⋯	⋯	92.5
4395.031	Ti II	1.08	−0.540	⋯	⋯	⋯	⋯	⋯	110.9
4395.839	Ti II	1.24	−1.930	⋯	⋯	⋯	⋯	⋯	45.5
4398.013	Y II	0.13	−1.000	⋯	⋯	⋯	⋯	⋯	17.7
4399.765	Ti II	1.24	−1.200	56.7	⋯	92.3	78.7	⋯	83.9
4400.399	Sc II	0.60	−0.540	42.3	31.7	⋯	⋯	⋯	71.8
4404.750	Fe I	1.56	−0.147	⋯	140.1	⋯	175.8	⋯	⋯
4407.709	Fe I	2.18	−1.970	⋯	⋯	91.1	⋯	⋯	73.8
4408.414	Fe I	2.20	−1.770	⋯	⋯	⋯	68.4	⋯	79.8
4415.123	Fe I	1.61	−0.615	⋯	115.5	⋯	⋯	⋯	⋯
4415.563	Sc II	0.59	−0.670	44.1	27.7	67.1	63.4	⋯	65.7
4416.830	Fe II	2.78	−2.540	34.4	⋯	39.3	51.5	⋯	56.2
4417.719	Ti II	1.17	−1.190	⋯	81.5	82.4	89.8	⋯	83.8
4418.331	Ti II	1.24	−1.990	33.3	30.6	39.9	⋯	⋯	49.0
4422.568	Fe I	2.85	−1.110	⋯	⋯	66.1	58.1	⋯	65.6
4425.441	Ca I	1.88	−0.360	80.3	65.6	98.9	88.1	⋯	87.2
4427.310	Fe I	0.05	−2.924	92.7	⋯	⋯	93.0	⋯	97.0
4430.614	Fe I	2.22	−1.659	54.6	⋯	72.7	55.9	⋯	66.1
4434.957	Ca I	1.89	−0.005	⋯	⋯	⋯	108.2	⋯	⋯
4442.339	Fe I	2.20	−1.255	80.3	53.2	109.1	77.7	127.6	87.5
4443.194	Fe I	2.86	−1.040	⋯	39.7	65.5	⋯	77.0	63.5
4443.801	Ti II	1.08	−0.710	93.8	88.6	107.7	104.9	113.7	105.2
4444.554	Ti II	1.12	−2.200	⋯	⋯	39.6	⋯	46.3	36.8
4447.717	Fe I	2.22	−1.342	71.4	⋯	91.6	79.6	109.5	83.6
4450.482	Ti II	1.08	−1.520	57.1	57.5	71.7	77.0	82.9	79.0
4451.575	Mn I	2.89	0.278	⋯	⋯	⋯	⋯	45.8	39.8
4454.381	Fe I	2.83	−1.300	45.5	⋯	65.5	⋯	71.8	49.1
4454.780	Ca I	1.90	0.258	⋯	97.3	⋯	108.2	⋯	⋯
4455.887	Ca I	1.90	−0.530	79.1	⋯	96.6	80.5	106.3	79.7
4459.118	Fe I	2.18	−1.279	94.5	72.7	⋯	97.6	⋯	112.7
4461.653	Fe I	0.09	−3.210	83.9	58.6	97.9	82.6	99.4	74.7
4464.450	Ti II	1.16	−1.810	⋯	⋯	55.0	⋯	62.2	65.0
4466.552	Fe I	2.83	−0.600	81.0	64.6	83.5	74.3	96.5	91.3
4468.493	Ti II	1.13	−0.630	93.8	85.0	100.7	112.1	118.4	114.1
4470.835	Ti II	1.17	−2.280	⋯	⋯	⋯	42.2	⋯	42.9
4476.019	Fe I	2.85	−0.820	98.5	⋯	⋯	100.1	131.0	106.3
4482.170	Fe I	0.11	−3.501	⋯	104.2	⋯	⋯	⋯	⋯
4482.253	Fe I	2.22	−1.480	⋯	104.2	⋯	⋯	⋯	⋯
4484.220	Fe I	3.60	−0.860	32.0	⋯	48.1	42.4	65.4	48.6
4489.739	Fe I	0.12	−3.966	44.3	⋯	65.6	47.2	72.5	55.6
4494.563	Fe I	2.20	−1.136	86.6	62.2	97.0	82.3	115.9	94.8
4501.270	Ti II	1.12	−0.770	⋯	74.1	101.2	105.8	⋯	103.2
4508.288	Fe II	2.86	−2.440	⋯	41.3	⋯	65.4	62.9	65.9
4515.339	Fe II	2.84	−2.600	⋯	⋯	⋯	64.9	61.3	58.0
4518.021	Ti I	0.83	−0.250	⋯	⋯	40.6	⋯	53.5	34.8
4520.224	Fe II	2.81	−2.650	⋯	⋯	46.7	56.0	55.2	57.4
4522.634	Fe II	2.84	−2.250	⋯	49.9	⋯	80.3	⋯	81.7
4528.614	Fe I	2.18	−0.822	⋯	80.6	⋯	⋯	⋯	⋯
4531.148	Fe I	1.49	−2.155	⋯	51.3	⋯	⋯	⋯	71.7
4533.239	Ti I	0.85	0.540	60.7	37.1	80.3	56.9	77.0	57.7
4533.972	Ti II	1.24	−0.770	85.7	94.5	⋯	114.2	112.2	106.4
4534.776	Ti I	0.84	0.340	⋯	33.8	71.2	52.5	77.0	56.4
4544.687	Ti I	0.82	−0.450	⋯	⋯	50.9	⋯	62.6	⋯
4547.847	Fe I	3.55	−1.010	33.7	⋯	47.7	⋯	54.0	43.2
4548.763	Ti I	0.83	−0.280	⋯	20.6	43.2	⋯	56.1	30.1
4554.036	Ba II	0.00	0.172	100.9	88.0	121.4	133.9	144.6	139.9
4555.890	Fe II	2.83	−2.400	⋯	⋯	56.3	63.2	59.2	62.3
4563.770	Ti II	1.22	−0.960	77.9	68.3	99.5	100.5	102.4	99.2

Table 3
(Continued)

Wavelength (Å)	Species	L.E.P. (eV)	log *gf*	J0054 (mÅ)	J0147 (mÅ)	J2158 (mÅ)	J2350 (mÅ)	J1218 (mÅ)	J1046 (mÅ)
4571.096	Mg I	0.00	−5.688	59.6	49.2	77.7	45.9	82.8	54.2
4571.971	Ti II	1.57	−0.310	89.7	81.3	109.6	108.8	…	106.5
4580.056	Cr I	0.94	−1.650	…	…	…	21.9	46.9	30.3
4583.837	Fe II	2.81	−1.930	67.5	66.0	…	96.4	85.5	84.8
4589.915	Ti II	1.24	−1.790	48.3	41.9	58.6	69.4	65.9	62.1
4592.651	Fe I	1.56	−2.449	…	41.2	…	…	…	…
4600.740	Cr I	1.00	−1.250	…	…	49.6	30.3	50.1	34.6
4602.941	Fe I	1.49	−2.210	72.7	…	83.4	70.1	81.8	67.9
4626.170	Cr I	0.97	−1.330	…	…	43.0	17.3	47.5	32.2
4632.912	Fe I	1.61	−2.913	…	…	55.4	…	67.7	45.1
4637.503	Fe I	3.28	−1.390	…	…	…	…	61.5	35.7
4646.150	Cr I	1.03	−0.740	47.1	…	65.0	53.1	71.1	55.0
4652.150	Cr I	1.00	−1.040	46.1	…	61.2	…	67.5	44.4
4681.909	Ti I	0.05	−1.020	…	…	40.4	…	54.1	29.6
4702.991	Mg I	4.33	−0.440	…	117.9	…	121.0	…	144.2
4714.417	Ni I	3.38	0.250	…	29.6	67.0	46.1	82.8	59.2
4733.591	Fe I	1.49	−2.990	31.6	…	48.1	31.2	52.2	41.2
4736.772	Fe I	3.21	−0.750	60.3	40.2	77.5	62.8	90.8	…
4783.430	Mn I	2.30	0.044	33.4	17.1	57.1	44.7	78.3	56.7
4805.085	Ti II	2.06	−0.960	40.4	29.1	56.7	63.2	65.8	60.2
4823.520	Mn I	2.32	0.136	37.7	20.2	62.6	43.1	76.5	55.5
4871.318	Fe I	2.87	−0.360	88.1	80.9	113.3	93.0	…	102.4
4872.138	Fe I	2.88	−0.570	79.5	67.2	99.7	87.4	…	91.5
4878.132	Ca I	2.71	−0.164	…	70.9	127.5	113.7	…	118.0
4878.211	Fe I	2.88	−0.890	…	71.2	…	113.7	…	118.0
4890.755	Fe I	2.88	−0.390	92.4	62.7	…	87.2	…	109.7
4891.492	Fe I	2.85	−0.110	…	83.7	…	106.0	…	125.3
4903.310	Fe I	2.88	−0.930	67.6	46.3	87.6	67.9	98.8	73.6
4918.994	Fe I	2.87	−0.340	97.0	75.0	…	96.6	…	106.0
4920.502	Fe I	2.83	0.070	…	108.5	…	…	…	…
4923.930	Fe II	2.89	−1.260	74.3	83.6	92.2	108.4	105.0	108.0
4924.770	Fe I	2.28	−2.256	30.9	…	45.5	32.9	60.6	44.0
4934.086	Ba II	0.00	−0.160	102.2	87.6	141.0	133.2	151.3	…
4938.814	Fe I	2.88	−1.080	59.7	…	75.7	62.3	85.2	63.5
4939.687	Fe I	0.86	−3.340	49.4	34.8	62.2	47.1	68.8	56.0
4957.299	Fe I	2.85	−0.408	…	77.2	…	…	…	…
4966.088	Fe I	3.33	−0.870	46.6	…	64.8	…	81.0	60.7
4981.730	Ti I	0.85	0.570	66.3	51.3	80.0	60.5	91.6	72.5
4991.066	Ti I	0.84	0.450	…	36.5	79.3	…	…	72.9
4994.130	Fe I	0.92	−2.956	51.9	47.6	71.7	…	75.5	62.6
4999.501	Ti I	0.83	0.320	56.6	37.2	74.3	53.1	77.1	57.3
5006.119	Fe I	2.83	−0.610	85.8	64.9	108.3	83.7	…	95.3
5007.209	Ti I	0.82	0.170	78.2	53.9	102.6	74.7	110.7	87.8
5012.068	Fe I	0.86	−2.642	78.6	65.3	92.9	83.4	112.6	90.0
5014.942	Fe I	3.94	−0.300	52.5	…	62.8	51.8	73.2	58.5
5016.160	Ti I	0.85	−0.480	…	…	31.7	17.3	…	…
5018.450	Fe II	2.89	−1.100	94.4	85.8	…	…	…	125.1
5020.024	Ti I	0.84	−0.330	24.2	…	…	…	55.0	28.3
5031.021	Sc II	1.36	−0.400	21.8	…	37.9	37.5	43.7	38.5
5041.072	Fe I	0.96	−3.090	58.4	…	77.9	…	…	…
5049.820	Fe I	2.28	−1.344	72.2	54.0	84.8	71.4	97.5	79.8
5051.635	Fe I	0.92	−2.795	69.1	54.1	80.7	65.9	96.1	78.5
5064.651	Ti I	0.05	−0.940	38.5	…	51.9	33.2	59.1	38.8
5068.766	Fe I	2.94	−1.040	54.7	34.0	67.4	…	80.3	62.7
5079.740	Fe I	0.99	−3.220	50.2	37.0	60.4	45.4	69.6	54.0
5083.339	Fe I	0.96	−2.958	57.5	34.5	66.0	53.1	82.9	64.4
5098.698	Fe I	2.18	−2.026	57.2	32.3	…	…	…	…
5110.357	Fe I	3.57	−1.370	…	62.7	91.3	…	97.8	78.6
5123.720	Fe I	1.01	−3.068	58.1	…	71.5	56.0	80.3	60.1
5127.359	Fe I	0.92	−3.307	44.0	…	52.5	42.2	70.3	55.5
5129.156	Ti II	1.88	−1.340	31.2	23.6	50.9	45.3	56.0	52.9
5133.689	Fe I	4.18	0.140	62.4	43.7	86.0	67.9	97.7	73.1
5141.739	Fe I	2.42	−1.964	…	12.1	39.9	27.7	54.9	32.5

Table 3
(Continued)

Wavelength (Å)	Species	L.E.P. (eV)	log *gf*	J0054 (mÅ)	J0147 (mÅ)	J2158 (mÅ)	J2350 (mÅ)	J1218 (mÅ)	J1046 (mÅ)
5150.840	Fe I	0.99	−3.070	51.1	⋯	62.0	48.9	71.9	59.8
5151.911	Fe I	1.01	−3.322	38.4	⋯	52.8	42.8	61.1	48.5
5154.070	Ti II	1.57	−1.780	22.8	22.0	37.9	36.0	49.2	46.8
5162.273	Fe I	4.18	0.020	59.2	45.1	75.4	65.0	86.9	72.6
5166.282	Fe I	0.00	−4.195	56.1	31.5	70.9	40.9	75.7	57.0
5171.596	Fe I	1.49	−1.793	96.4	88.4	109.7	86.0	⋯	104.0
5185.902	Ti II	1.89	−1.350	29.8	21.5	43.4	44.9	⋯	42.8
5191.455	Fe I	3.04	−0.550	79.7	60.3	104.0	80.8	119.0	87.8
5192.344	Fe I	3.00	−0.420	84.1	65.5	109.7	84.4	123.3	93.1
5192.969	Ti I	0.02	−0.950	⋯	⋯	53.2	28.3	66.2	35.3
5194.942	Fe I	1.56	−2.090	75.4	62.6	86.0	73.7	91.8	74.6
5197.577	Fe II	3.23	−2.220	28.7	26.7	46.4	60.8	49.5	59.0
5198.711	Fe I	2.22	−2.135	⋯	30.6	56.2	41.5	64.6	49.1
5202.336	Fe I	2.18	−1.838	67.0	45.6	83.3	⋯	101.7	82.1
5204.583	Fe I	0.09	−4.332	⋯	82.9	128.8	101.5	155.5	117.2
5206.040	Cr I	0.94	0.020	96.9	73.5	107.7	91.1	144.0	103.4
5208.420	Cr I	0.94	0.170	⋯	90.4	⋯	⋯	⋯	⋯
5210.384	Ti I	0.05	−0.820	50.6	⋯	56.7	31.0	68.7	38.3
5216.274	Fe I	1.61	−2.150	63.9	45.1	73.2	⋯	88.5	70.8
5217.390	Fe I	3.21	−1.070	40.3	⋯	59.8	⋯	77.2	53.6
5225.525	Fe I	0.11	−4.789	⋯	⋯	33.4	⋯	39.4	23.1
5226.543	Ti II	1.57	−1.230	54.0	36.5	68.6	⋯	71.0	66.7
5227.150	Fe I	2.42	−1.367	⋯	90.8	⋯	⋯	⋯	⋯
5227.189	Fe I	1.56	−1.230	⋯	90.8	⋯	⋯	⋯	⋯
5232.940	Fe I	2.94	−0.060	113.6	85.8	⋯	⋯	⋯	⋯
5234.630	Fe II	3.22	−2.180	32.0	29.7	43.5	⋯	57.7	62.3
5250.646	Fe I	2.20	−2.180	⋯	⋯	66.6	⋯	66.8	52.8
5254.956	Fe I	0.11	−4.764	⋯	⋯	⋯	⋯	53.4	39.9
5266.555	Fe I	3.00	−0.390	91.0	74.9	114.5	94.2	⋯	99.8
5269.537	Fe I	0.86	−1.321	⋯	130.8	⋯	⋯	⋯	152.6
5270.356	Fe I	1.61	−1.510	⋯	123.4	⋯	⋯	⋯	⋯
5276.002	Fe II	3.20	−2.010	44.8	32.6	64.9	77.6	84.7	78.2
5281.790	Fe I	3.04	−0.830	64.8	46.4	82.1	56.2	88.3	72.4
5283.630	Fe I	3.24	−0.524	83.3	57.5	98.5	69.8	114.2	85.8
5298.280	Cr I	0.98	−1.140	36.5	⋯	60.5	⋯	⋯	⋯
5302.300	Fe I	3.28	−0.720	59.6	⋯	76.3	61.4	89.8	62.4
5307.361	Fe I	1.61	−2.987	28.9	15.1	46.8	⋯	51.0	37.5
5316.615	Fe II	3.15	−1.870	53.0	45.5	⋯	⋯	⋯	⋯
5324.179	Fe I	3.21	−0.103	102.8	⋯	⋯	102.6	⋯	102.8
5328.039	Fe I	0.92	−1.466	⋯	112.9	⋯	118.3	⋯	⋯
5328.531	Fe I	1.56	−1.850	84.1	69.4	⋯	⋯	⋯	⋯
5332.900	Fe I	1.56	−2.780	41.5	⋯	49.7	36.5	60.1	44.2
5476.904	Ni I	1.83	−0.780	76.6	63.9	93.4	72.0	106.8	80.2
5497.516	Fe I	1.01	−2.849	65.5	42.1	83.4	69.1	88.7	73.0
5501.465	Fe I	0.96	−3.050	59.9	43.9	66.0	57.1	79.0	65.2
5506.778	Fe I	0.99	−2.797	67.2	47.1	82.6	61.5	94.1	71.9
5526.790	Sc II	1.77	0.020	23.7	14.3	39.7	38.8	44.9	42.7
5528.404	Mg I	4.35	−0.498	⋯	105.5	⋯	120.6	⋯	131.4
5534.847	Fe II	3.25	−2.750	⋯	⋯	27.1	33.7	31.0	32.2
5569.618	Fe I	3.42	−0.540	59.5	42.2	87.1	62.4	95.9	73.6
5572.842	Fe I	3.40	−0.275	79.1	53.5	⋯	72.9	125.0	89.0
5576.088	Fe I	3.43	−1.000	47.0	35.9	58.2	46.2	⋯	⋯
5586.755	Fe I	3.37	−0.096	91.8	57.8	117.2	80.4	⋯	98.0
5588.757	Ca I	2.53	0.358	85.6	64.3	98.5	82.4	120.1	92.2
5594.468	Ca I	2.52	0.097	71.2	57.1	85.4	81.5	⋯	89.6
5598.487	Ca I	2.52	−0.087	68.7	50.0	⋯	⋯	⋯	79.1
5615.644	Fe I	3.33	0.050	107.7	⋯	⋯	103.4	⋯	113.6
5853.688	Ba II	0.60	−1.026	18.4	15.3	33.3	39.6	39.4	48.0
5857.452	Ca I	2.93	0.240	66.8	45.6	82.0	62.2	100.6	72.3
5889.951	Na I	0.00	0.101	241.9	182.2	310.8	255.6	408.4	252.2
5895.924	Na I	0.00	−0.197	198.8	155.9	267.0	224.0	309.9	219.4
6102.722	Ca I	1.88	−0.770	68.9	44.0	91.1	65.2	105.6	72.1
6122.219	Ca I	1.89	−0.320	107.2	68.9	126.7	95.1	142.6	106.5

Table 3
(Continued)

Wavelength (Å)	Species	L.E.P. (eV)	log *gf*	J0054 (mÅ)	J0147 (mÅ)	J2158 (mÅ)	J2350 (mÅ)	J1218 (mÅ)	J1046 (mÅ)
6136.614	Fe I	2.45	−1.400	72.7	53.2	79.8	74.7	90.0	79.7
6137.691	Fe I	2.59	−1.403	63.1	41.6	76.7	63.9	84.7	72.1
6141.730	Ba II	0.70	−0.070	58.2	49.2	71.3	78.0	80.5	92.0
6162.172	Ca I	1.90	−0.090	122.8	85.0	142.4	104.5	…	132.5
6191.558	Fe I	2.43	−1.420	59.1	…	…	66.6	87.5	…
6230.723	Fe I	2.56	−1.281	73.3	47.1	87.4	72.8	98.9	80.9
6252.560	Fe I	2.40	−1.767	54.0	42.0	69.6	53.7	86.9	66.7
6265.130	Fe I	2.18	−2.540	27.3	…	40.8	…	52.1	35.2
6301.500	Fe I	3.65	−0.720	…	…	41.2	…	…	…
6335.330	Fe I	2.20	−2.180	40.7	…	53.7	40.2	65.2	45.9
6393.601	Fe I	2.43	−1.432	67.3	46.6	79.1	60.6	89.3	69.7
6421.350	Fe I	2.28	−2.027	49.6	32.4	62.5	51.1	74.8	60.5
6430.845	Fe I	2.18	−2.006	53.4	32.9	69.3	50.4	75.9	65.7
6439.073	Ca I	2.53	0.390	93.4	78.3	109.9	96.4	…	…
6462.566	Ca I	2.52	0.262	103.4	67.1	…	101.9	…	111.4
6493.780	Ca I	2.52	−0.109	63.6	49.0	82.5	67.2	98.3	75.3
6494.980	Fe I	2.40	−1.239	81.9	71.0	92.0	76.7	107.4	83.1
6496.908	Ba II	0.60	−0.407	46.9	39.7	67.5	69.3	…	72.0
6592.910	Fe I	2.73	−1.473	47.1	29.1	64.8	39.4	67.4	60.6
6643.630	Ni I	1.68	−2.220	13.4	…	35.5	16.0	55.4	30.0
6677.987	Fe I	2.69	−1.470	62.9	40.3	74.2	58.2	88.0	68.8
6707.761	Li I	0.00	0.174	…	…	1.2	…	1.9	44.2
4600.752	Cr I	1.00	−1.260	…	…	49.6	30.3	50.1	34.6
4604.994	Ni I	3.48	−0.290	…	…	…	…	45.2	32.6
4611.185	Fe I	2.85	−2.720	…	…	…	…	74.7	…
4616.137	Cr I	0.98	−1.190	32.8	…	51.0	…	57.9	38.5
4618.758	Fe I	2.95	−2.410	…	…	…	47.8	59.0	…
4619.287	Fe I	3.60	−1.120	…	…	45.5	…	52.2	42.5
4620.513	Fe II	2.83	−3.290	…	…	…	27.3	…	27.8
4625.045	Fe I	3.24	−1.340	…	…	47.6	…	53.6	43.0
4626.188	Cr I	0.97	−1.320	…	…	43.0	…	47.5	32.2
4637.503	Fe I	3.28	−1.390	…	…	…	…	61.5	35.7
4647.435	Fe I	2.95	−1.350	39.8	…	…	…	62.0	47.5
4648.659	Ni I	3.42	−0.160	…	11.9	38.0	…	64.7	37.0
4651.285	Cr I	0.98	−1.460	…	…	38.8	…	49.4	27.3
4656.468	Ti I	0.00	−1.289	…	…	…	…	52.7	21.2
4670.406	Sc II	1.36	−0.580	17.4	…	28.6	…	30.6	28.4
4678.846	Fe I	3.60	−0.830	…	…	…	43.9	65.7	52.9
4691.411	Fe I	2.99	−1.520	35.3	…	62.4	…	…	53.6
4707.274	Fe I	3.24	−1.080	…	…	…	…	73.3	62.1
4708.651	Ti II	1.24	−2.370	…	…	…	…	38.2	33.2
4710.283	Fe I	3.02	−1.610	…	…	53.6	…	56.9	37.7
4731.439	Fe II	2.89	−3.360	…	…	…	35.0	47.7	36.9
4741.529	Fe I	2.83	−1.760	…	…	…	…	40.5	28.1
4779.979	Ti II	2.05	−1.370	…	23.2	…	39.6	48.9	40.9
4786.807	Fe I	3.02	−1.610	…	…	43.8	…	…	36.0
4789.650	Fe I	3.55	−0.960	…	…	…	30.4	53.8	38.1
4798.507	Ti II	1.08	−2.670	…	…	…	…	28.3	22.4
4829.028	Ni I	3.54	−0.330	…	…	…	…	49.2	30.4
4831.183	Ni I	3.61	−0.420	…	…	…	…	44.3	…
4840.873	Ti I	0.90	−0.453	…	…	32.4	…	42.7	26.6
4855.414	Ni I	3.54	0.000	25.2	16.3	…	…	…	…
4904.413	Ni I	3.54	−0.170	20.5	…	36.6	29.3	50.8	33.2
4924.770	Fe I	2.28	−2.256	30.9	…	45.5	32.9	60.6	44.0
4973.102	Fe I	3.96	−0.950	24.7	…	39.4	26.5	50.3	34.3
4978.604	Fe I	3.98	−0.930	…	…	36.3	…	46.4	28.5
4980.161	Ni I	3.61	−0.110	24.0	…	43.0	36.8	58.7	35.9
5022.236	Fe I	3.98	−0.530	36.2	…	50.7	42.4	69.9	47.3
5028.127	Fe I	3.57	−1.120	20.2	…	35.2	…	45.9	39.6
5035.374	Ni I	3.63	0.290	33.7	26.3	52.7	36.0	71.2	50.7
5035.902	Ti I	1.46	0.260	32.9	…	56.5	31.5	75.6	39.3
5036.463	Ti I	1.44	0.186	24.4	…	40.2	…	50.1	30.2
5074.749	Fe I	4.22	−0.200	…	…	64.8	49.8	69.8	56.9

Table 3
(Continued)

Wavelength (Å)	Species	L.E.P. (eV)	log *gf*	J0054 (mÅ)	J0147 (mÅ)	J2158 (mÅ)	J2350 (mÅ)	J1218 (mÅ)	J1046 (mÅ)
5079.224	Fe I	2.20	−2.067	46.9	⋯	60.9	41.3	⋯	⋯
5080.523	Ni I	3.65	0.130	25.5	23.4	56.3	38.6	74.2	47.1
5090.773	Fe I	4.26	−0.400	⋯	⋯	40.4	30.0	48.8	35.1
5125.117	Fe I	4.22	−0.140	⋯	⋯	70.6	⋯	⋯	62.0
5131.468	Fe I	2.22	−2.510	⋯	⋯	40.1	⋯	50.5	35.1
5137.075	Ni I	1.68	−1.990	31.4	15.0	47.8	29.0	61.5	34.5
5137.382	Fe I	4.18	−0.400	32.2	18.7	52.2	43.0	66.2	51.3
5141.739	Fe I	2.42	−1.964	⋯	12.1	39.9	27.7	54.9	32.5
5173.740	Ti I	0.00	−1.062	⋯	⋯	⋯	17.1	⋯	39.4
5235.385	Fe I	4.08	−0.970	⋯	⋯	27.5	⋯	45.4	28.4
5242.491	Fe I	3.63	−0.970	⋯	19.6	43.8	⋯	53.0	40.2
5247.050	Fe I	0.09	−4.946	⋯	⋯	24.3	⋯	⋯	⋯
5247.564	Cr I	0.96	−1.640	⋯	⋯	31.0	⋯	42.2	⋯
5250.210	Fe I	0.12	−4.938	⋯	⋯	27.7	⋯	38.6	18.7
5261.706	Ca I	2.52	−0.579	39.0	⋯	56.1	43.5	70.4	45.3
5262.244	Ca I	2.52	−0.471	48.8	32.8	78.3	57.5	97.2	69.5
5263.305	Fe I	3.27	−0.879	⋯	23.1	68.1	53.5	82.9	58.9
5265.557	Ca I	2.52	−0.113	65.3	43.2	⋯	⋯	⋯	⋯
5296.686	Cr I	0.98	−1.400	⋯	⋯	51.9	⋯	57.7	32.2
5336.778	Ti II	1.58	−1.630	⋯	⋯	48.3	46.0	⋯	⋯
5463.276	Fe I	4.43	0.110	33.2	⋯	50.9	40.0	66.5	49.1
5466.390	Fe I	4.37	−0.630	15.4	⋯	31.8	⋯	39.1	29.3
5476.563	Fe I	4.10	−0.450	36.4	⋯	57.9	39.8	⋯	45.5
5487.744	Fe I	4.14	−0.710	⋯	⋯	35.2	⋯	49.8	30.4
5512.979	Ca I	2.93	−0.447	34.7	⋯	43.0	30.4	59.5	36.9
5534.834	Fe II	3.25	−2.930	11.7	⋯	27.1	33.7	31.0	32.2
5563.599	Fe I	4.19	−0.990	19.7	⋯	31.8	⋯	45.8	27.2
5581.971	Ca I	2.52	−0.555	42.9	25.0	52.3	39.2	68.0	48.0
5590.120	Ca I	2.52	−0.571	37.0	23.6	51.1	48.8	66.6	44.8
5601.285	Ca I	2.53	−0.523	39.4	⋯	60.4	50.3	74.1	49.4
5615.294	Fe I	2.59	−2.453	⋯	⋯	⋯	⋯	48.4	⋯
5624.542	Fe I	3.42	−0.755	49.9	⋯	64.2	50.9	87.0	62.7
5658.816	Fe I	3.40	−0.793	49.3	37.1	71.6	⋯	⋯	61.6
5567.390	Fe I	2.61	−2.564	⋯	⋯	⋯	8.7	⋯	⋯
5638.266	Fe I	4.22	−0.870	⋯	⋯	20.9	⋯	38.4	26.4
5641.000	Sc II	1.50	−1.130	⋯	⋯	⋯	⋯	16.1	11.3
5657.907	Sc II	1.51	−0.600	⋯	13.4	30.0	20.3	35.9	31.6
5667.164	Sc II	1.50	−1.310	⋯	2.5	⋯	6.1	⋯	7.2
5669.055	Sc II	1.50	−1.200	⋯	⋯	⋯	⋯	15.9	12.7
5682.633	Na I	2.10	−0.700	⋯	⋯	24.1	30.3	47.5	25.8
5688.204	Na I	2.10	−0.460	⋯	⋯	48.0	49.5	64.6	37.8
5701.543	Fe I	2.56	−2.216	24.3	⋯	35.6	24.2	45.5	30.8
5711.088	Mg I	4.35	−1.720	39.6	39.3	65.7	30.1	75.6	48.2
5711.867	Fe I	4.28	−1.460	⋯	⋯	⋯	⋯	35.9	19.8
5753.123	Fe I	4.26	−0.690	⋯	⋯	30.1	⋯	37.5	24.9
5754.675	Ni I	1.94	−2.330	⋯	⋯	⋯	⋯	37.4	17.6
5762.992	Fe I	4.21	−0.450	39.7	⋯	52.5	31.6	67.8	47.4
5857.452	Ca I	2.93	0.240	66.8	45.6	82.0	62.2	100.6	72.3
5866.448	Ti I	1.07	−0.784	⋯	⋯	22.9	⋯	⋯	7.8
5916.246	Fe I	2.45	−2.994	⋯	⋯	11.8	⋯	20.6	⋯
5930.173	Fe I	4.65	−0.230	⋯	⋯	⋯	⋯	52.6	42.5
5934.658	Fe I	3.93	−1.170	12.6	⋯	⋯	⋯	36.3	22.2
6003.033	Fe I	3.88	−1.120	⋯	⋯	29.8	⋯	46.6	27.3
6024.066	Fe I	4.55	−0.120	36.6	22.6	48.4	36.1	⋯	⋯
6213.429	Fe I	2.22	−2.480	23.1	⋯	39.2	19.7	51.3	31.9
6219.280	Fe I	2.20	−2.433	31.2	⋯	50.1	34.5	56.2	38.3
6246.318	Fe I	3.60	−0.733	40.3	⋯	57.1	⋯	78.4	48.8
6247.545	Fe II	3.89	−2.510	⋯	⋯	⋯	⋯	22.6	28.1
6254.257	Fe I	2.28	−2.443	35.2	⋯	54.3	⋯	69.4	48.6
6336.835	Fe I	3.69	−1.050	35.2	⋯	52.4	38.3	64.9	46.6
6355.029	Fe I	2.85	−2.365	12.3	⋯	⋯	⋯	⋯	⋯
6408.020	Fe I	3.69	−1.018	27.9	⋯	⋯	31.4	53.8	32.2
6411.649	Fe I	3.65	−0.595	36.3	31.7	⋯	43.4	82.7	⋯

Table 3
(Continued)

Wavelength (Å)	Species	L.E.P. (eV)	log *gf*	J0054 (mÅ)	J0147 (mÅ)	J2158 (mÅ)	J2350 (mÅ)	J1218 (mÅ)	J1046 (mÅ)
6419.982	Fe I	4.73	−0.240	⋯	⋯	⋯	⋯	49.1	31.1
6432.682	Fe II	2.89	−3.550	⋯	⋯	⋯	⋯	⋯	14.8
6449.810	Ca I	2.52	−0.502	48.9	⋯	62.5	44.9	76.9	51.7
6456.389	Fe II	3.90	−2.300	⋯	⋯	⋯	30.6	27.4	35.9
6471.660	Ca I	2.53	−0.686	40.6	⋯	52.7	37.4	68.5	48.3
6475.624	Fe I	2.56	−2.940	⋯	⋯	13.0	⋯	21.7	⋯
6491.697	Mn I	3.76	−1.040	⋯	⋯	⋯	15.5	⋯	⋯
6499.649	Ca I	2.52	−0.818	31.0	25.7	53.4	29.0	63.0	32.0
6546.238	Fe I	2.76	−1.540	42.5	29.5	63.6	45.7	68.5	51.3
6593.868	Fe I	2.43	−2.422	28.8	⋯	⋯	⋯	50.4	27.4
6604.578	Sc II	1.36	−1.310	4.1	⋯	⋯	⋯	16.5	⋯
6663.440	Fe I	2.42	−2.479	⋯	⋯	⋯	⋯	49.2	30.1
6717.685	Ca I	2.71	−0.524	39.8	28.0	55.9	39.9	76.8	52.5
6750.151	Fe I	2.42	−2.621	⋯	⋯	25.1	⋯	41.5	23.0
6767.778	Ni I	1.83	−2.170	23.1	⋯	32.8	18.6	44.4	⋯

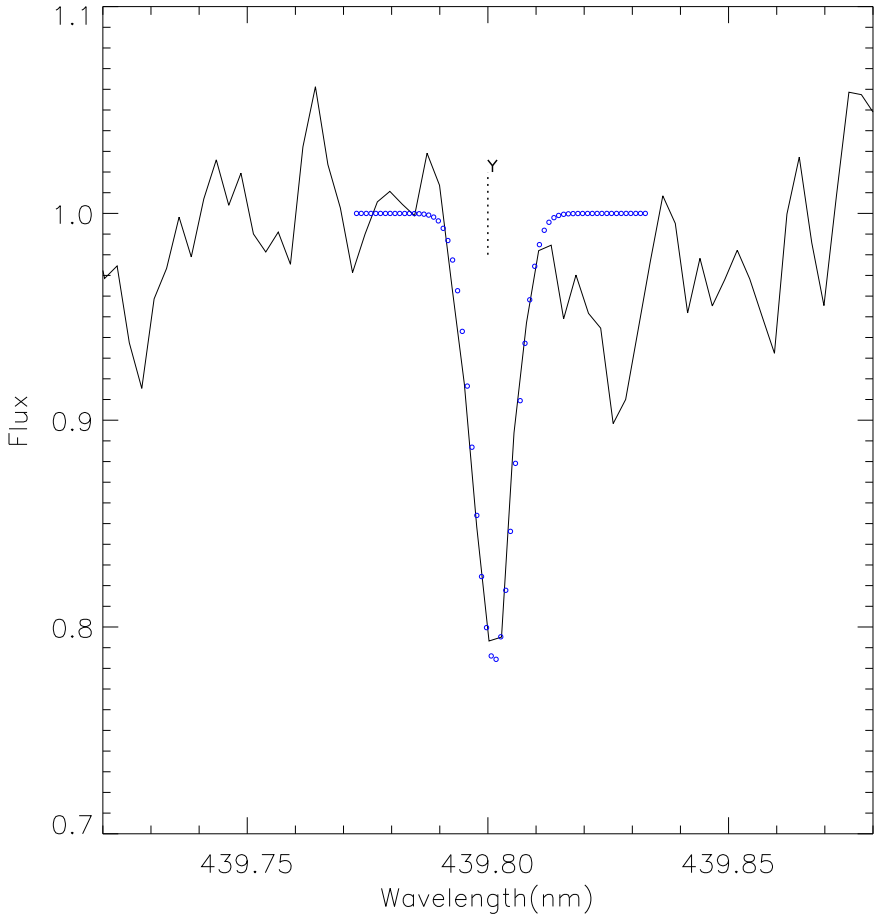

Figure 4. Example of the Y element determination by spectra fitting. The black line is the observed spectrum and the open circles represent the theoretical spectrum.

4. Results

4.1. α-elements

Figure 6 compares [α/Fe] in LAMOST-N1 to field stars in the Milky Way. [α/Fe] is derived by the average of the [Mg/Fe] and [Ca/Fe]. The six member stars are marked by red squares. The field stars (open circles) and stars of four dSphs (triangles) are extracted from the SAGA database (Suda et al. 2008).[8] These dSphs include Draco, Fornax, Ursa Minor, and Sagittarius, and are distinguished by different colors. Among these dSphs, Sagittarius stars show a wide [Fe/H] distribution from −1.5 to −0.1. In addition, the three

[8] http://sagadatabase.jp/

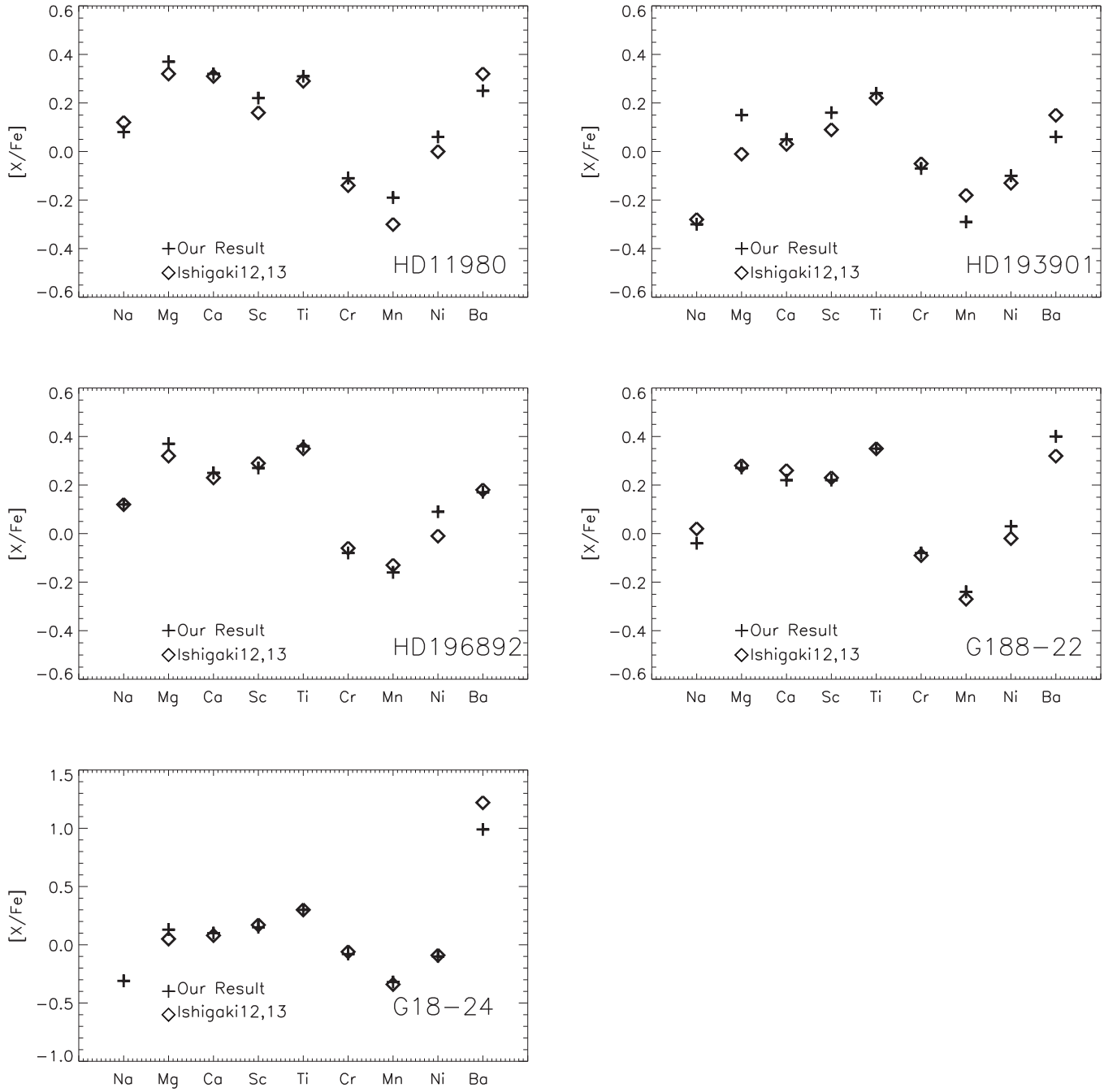

Figure 5. Abundance comparison for five calibration stars between our results and those in Ishigaki et al. (2012). The plus signs represent the [X/Fe] of our results, while the diamonds represent [X/Fe] from Ishigaki et al. (2012).

Table 4
[X/Fe] Abundances for Our Six Stars and Five Comparison Stars

Id	[Na/Fe]	[Mg/Fe]	[Ca/Fe]	[Sc/Fe]	[Ti/Fe]	[Cr/Fe]	[Mn/Fe]	[Ni/Fe]	[Ba/Fe]	[Y/Fe]
J0054+3047	−0.37	0.35	0.16	0.13	0.34	−0.19	−0.47	−0.10	0.04	−0.15
J0147+2742	−0.09	0.19	0.15	−0.17	0.19	−0.18	−0.60	−0.16	−0.13	
J1046+5004	−0.18	0.21	0.04	0.20	0.31	−0.14	−0.38	−0.01	0.02	−0.15
J1218+2852	−0.05	0.06	0.15	0.03	0.14	−0.15	−0.25	−0.09	0.14	−0.24
J2158+2840	−0.20	0.34	0.06	0.24	0.35	−0.07	−0.37	−0.06	0.06	−0.18
J2350+2622	0.22	0.14	0.22	0.04	0.20	−0.06	−0.28	−0.04	0.07	−0.12
G18-24	−0.31	0.13	0.10	0.15	0.34	−0.08	−0.32	−0.10	0.99	···
G188-22	−0.04	0.27	0.22	0.22	0.44	−0.08	−0.24	0.03	0.40	···
HD 193901	−0.30	0.15	0.05	0.16	0.34	−0.07	−0.29	−0.10	0.06	···
HD 196892	0.12	0.37	0.25	0.27	0.41	−0.08	−0.16	0.09	0.17	···
HD 111980	0.08	0.37	0.32	0.22	0.36	−0.11	−0.19	0.06	0.25	···

Table 5
Uncertainties of the Abundance Measurement for J0054+3047, J0147+2742, and J2158+2840

	J0054+3047						J0147+2742						J2158+2840					
Δ[X/H]	$\frac{\sigma \mathrm{EW}}{\sqrt{N}}$	T_{eff} +100 K (K)	log g +0.15 (dex)	[Fe/H] +0.15 (dex)	ξ_t +0.2 (km s^{-1})	σ Total	$\frac{\sigma \mathrm{EW}}{\sqrt{N}}$	T_{eff} +100 K (K)	log g +0.15 (dex)	[Fe/H] +0.15 (dex)	ξ_t +0.2 (km s^{-1})	σ Total	$\frac{\sigma \mathrm{EW}}{\sqrt{N}}$	T_{eff} +100 K (K)	log g +0.15 (dex)	[Fe/H] +0.15 (dex)	ξ_t +0.2 (km s^{-1})	σ Total
Ba II	0.04	0.08	0.01	0.02	−0.03	0.10	0.05	0.07	0.03	0.01	−0.07	0.12	0.03	0.07	0.07	0.11	0.04	0.16
Ca I	0.03	0.08	−0.03	0.00	−0.01	0.09	0.04	0.06	−0.02	0.00	−0.03	0.08	0.03	0.09	0.04	0.09	0.07	0.15
Cr I	0.04	0.11	−0.02	0.00	−0.01	0.12	0.03	0.14	−0.04	0.01	−0.08	0.17	0.04	0.11	0.08	0.11	0.09	0.20
Fe I	0.03	0.09	−0.03	0.00	−0.03	0.10	0.04	0.09	−0.02	0.00	−0.05	0.11	0.04	0.10	0.07	0.11	0.07	0.18
Fe II	0.05	0.02	0.03	0.02	−0.02	0.07	0.04	0.01	0.04	0.00	−0.05	0.08	0.04	0.01	0.04	0.03	−0.02	0.07
Mg I	0.03	0.09	−0.01	0.00	−0.01	0.10	0.02	0.07	−0.03	0.00	−0.02	0.08	0.03	0.10	0.08	0.10	0.08	0.18
Mn I	0.03	0.08	−0.02	−0.01	−0.01	0.09	0.06	0.07	0.00	0.00	−0.01	0.09	0.03	0.10	0.06	0.11	0.08	0.18
Na I	0.03	0.08	−0.04	0.00	0.00	0.09	0.07	0.09	−0.04	0.01	−0.02	0.12	0.02	0.08	0.03	0.09	0.07	0.14
Ni I	0.04	0.07	−0.01	−0.01	−0.01	0.08	0.05	0.06	0.00	0.00	−0.02	0.08	0.04	0.09	0.07	0.09	0.07	0.17
Sc II	0.07	0.04	0.05	0.02	−0.01	0.10	0.10	0.04	0.05	0.01	−0.01	0.12	0.04	0.03	0.07	0.05	0.00	0.10
Ti I	0.04	0.10	−0.03	−0.01	−0.03	0.12	0.04	0.09	0.00	0.00	−0.03	0.10	0.04	0.12	0.09	0.11	0.08	0.21
Ti II	0.03	0.04	0.02	0.01	−0.03	0.06	0.04	0.04	0.03	0.00	−0.06	0.09	0.04	0.04	0.06	0.07	0.00	0.11

Table 6
Uncertainties of the Abundance for J2350+2622, J1218+2852, and J1046+5004

	J2350+2622						J1218+2852						J1046+5004					
Δ[X/H]	$\frac{\sigma EW}{\sqrt{N}}$	T_{eff} +100 K (K)	log g +0.15 (dex)	[Fe/H] +0.15 (dex)	ξ_t +0.2 (km s^{-1})	σ Total	$\frac{\sigma EW}{\sqrt{N}}$	T_{eff} +100 K (K)	log g +0.15 (dex)	[Fe/H] +0.15 (dex)	ξ_t +0.2 (km s^{-1})	σ Total	$\frac{\sigma EW}{\sqrt{N}}$	T_{eff} +100 K (K)	log g +0.15 (dex)	[Fe/H] +0.15 (dex)	ξ_t +0.2 (km s^{-1})	σ Total
Ba II	0.06	0.07	0.03	0.01	−0.07	0.12	0.06	0.07	0.02	0.02	−0.07	0.12	0.05	0.06	0.00	0.07	−0.03	0.11
Ca I	0.07	0.07	−0.01	0.01	−0.03	0.10	0.07	0.07	−0.02	0.00	−0.03	0.11	0.04	0.08	−0.05	0.01	−0.02	0.10
Cr I	0.08	0.09	0.00	0.00	−0.02	0.12	0.07	0.09	−0.01	0.00	−0.03	0.12	0.07	0.11	−0.03	0.01	−0.03	0.14
Fe I	0.08	0.08	−0.01	0.00	−0.04	0.12	0.08	0.09	−0.01	0.00	−0.04	0.13	0.06	0.09	−0.04	0.00	−0.04	0.12
Fe II	0.08	0.02	0.05	0.01	−0.04	0.10	0.08	0.01	0.04	0.01	−0.05	0.10	0.08	0.00	0.03	0.03	−0.04	0.10
Mg I	0.05	0.08	−0.03	0.01	−0.02	0.10	0.05	0.08	−0.04	0.00	−0.02	0.10	0.05	0.10	−0.03	0.00	−0.02	0.12
Mn I	0.08	0.06	−0.01	0.00	−0.02	0.10	0.07	0.08	−0.02	0.00	−0.03	0.11	0.06	0.09	−0.04	0.01	−0.02	0.12
Na I	0.05	0.07	−0.03	0.01	−0.01	0.09	0.05	0.08	−0.03	0.01	−0.01	0.10	0.03	0.08	−0.05	0.01	0.00	0.10
Ni I	0.09	0.07	0.00	0.01	−0.01	0.11	0.08	0.07	−0.01	0.00	−0.03	0.11	0.06	0.08	−0.03	0.01	−0.03	0.11
Sc II	0.11	0.04	0.05	0.01	−0.01	0.13	0.11	0.04	0.05	0.02	−0.04	0.13	0.09	0.01	0.05	0.02	−0.02	0.11
Ti I	0.08	0.09	0.00	0.01	−0.02	0.12	0.09	0.10	0.00	0.00	−0.03	0.14	0.07	0.11	−0.03	0.00	−0.05	0.14
Ti II	0.07	0.04	0.04	0.00	−0.06	0.11	0.08	0.04	0.04	0.01	−0.06	0.12	0.07	0.04	0.03	0.04	−0.04	0.10

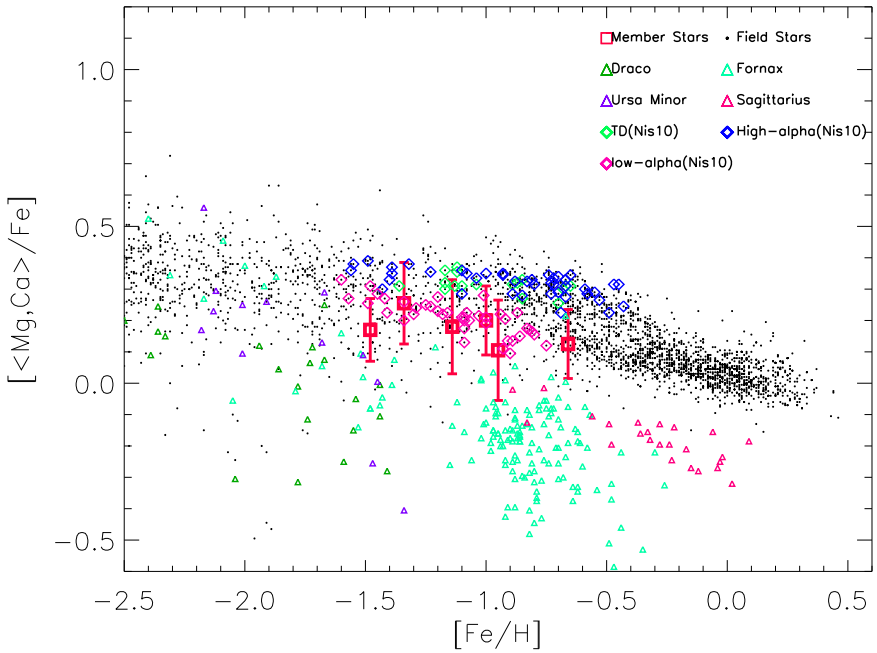

Figure 6. [α/Fe] vs. [Fe/H]. The red squares represent the member stars of LAMOST-N1. The open circles are field stars of the Milky Way from the SAGA database. Green diamonds are stars in the thick disk from Nis10. Halo stars with high-α are marked with blue diamonds from Nis10. The magenta diamonds represent the halo stars with low-α from Nis10. Stars of the dwarf galaxies are shown with triangles. Dwarf galaxies are distinguished by different colors.

populations of Nissen & Schuster (2010) are also plotted in this figure. In general, the α abundance of dSph stars is over 0.1 dex, lower than that of Galactic stars with the same [Fe/H]. [α/Fe] of most dSph stars exhibit a sub-solar value. The [α/Fe] of the member stars of LAMOST-N1 shows a similar distribution with that of low-α halo populations and separates well from the thick-disk population and high-α halo populations of Nissen & Schuster (2010).

4.2. Sodium and Iron-peak Elements

Figure 7 plots the abundance trend of Na and Ni as a function of metallicity ([Fe/H]). The abundance ratio of field stars (open circles) and dSphs stars (triangles) are from the SAGA database (Suda et al. 2008). For stars with [Fe/H] < -1.0, [Na/Fe] and [Ni/Fe] show larger scatter. Most stars of dSph have negative [Na/Fe] ratios. Six member stars of LAMOST-N1 exhibit a large dispersion of [Na/Fe], five stars are with negative [Na/Fe], and only one star exhibits higher [Na/Fe] than solar value. [Ni/Fe] of those six stars are all lower than the solar value and demonstrate a function of [Fe/H] in which lower [Ni/Fe] correspond to lower [Fe/H]. The relationship between Na and Ni abundances also can be used to discriminate different populations (Nissen & Schuster 2010). In summary, an Na–Ni correlation is expected when the chemical enrichment is dominated by SNe II because the production of ^{23}Na and ^{58}Ni depends on the neutron excess. Figure 8 shows the Na–Ni values for Galactic field stars, stars of dSphs, and stars in LAMOST-N1. In addition, three different populations of thick-disk, high-α halo, and low-α halo stars from Nissen & Schuster (2010) have also been plotted as diamonds with different colors. The high-α and low-α halo populations are well separated.

Figure 9 displays the Sc, Cr, and Mn abundance distribution. Abundance results of field stars (open circles) and dSphs stars (triangles) are from the SAGA database (Suda et al. 2008). For these three elements, an increasing trend of [X/Fe] with increasing [Fe/H] is clearly found in the six member stars of LAMOST-N1. Among the three elements, the [Cr/Fe] of the member stars is lower than those of field stars. The Cr abundances are determined by Cr I lines for our member stars and the use of Cr I lines would underestimate the overall Cr abundance (Ishigaki et al. 2013). As for field stars from Bensby et al. (2014), the Cr abundances are determined from both neutral and ionized lines. Ishigaki et al. (2014) presented chemical compositions of six metal-poor stars in the ultra-faint dSph Boötes I and found lower [Cr/Fe] ratios for some stars. Thus, another possibility is the progenitor of LAMOST-N1 is with lower [Cr/Fe] ratios.

4.3. Neutron-capture Elements

[Ba/Y] exhibits the difference between dSph stars and Galactic field stars (Venn et al. 2004), which tends to be significantly high/offset in dSph stars than in the Galactic field stars. This was interpreted as due to differences in the star formation history (SFH) in the dSphs, leading to asymptotic giant branch (AGB) contributions in the dSphs from a more homogeneous sample of stars (mass and metallicity) compared to the Galaxy. Figure 10 plots the [Ba/Y] versus [Fe/H] for the five member stars in LAMOST-N1, stars in dSph, and Galactic field stars, plus three different populations of thick-disk, high-α halo, and low-α halo stars from Nissen & Schuster (2011). It is evident that the [Ba/Y] ratio of member stars is lower than the dSphs and higher than the Galactic field stars.

5. Discussion

Generally, there are three types for streams or moving groups. One is the relics of clusters, and another is the remnants of the dSph. These two types are caused by the gravitational interaction with the Milky Way and are usually called tidal streams. The third type is the result of the perturbation of

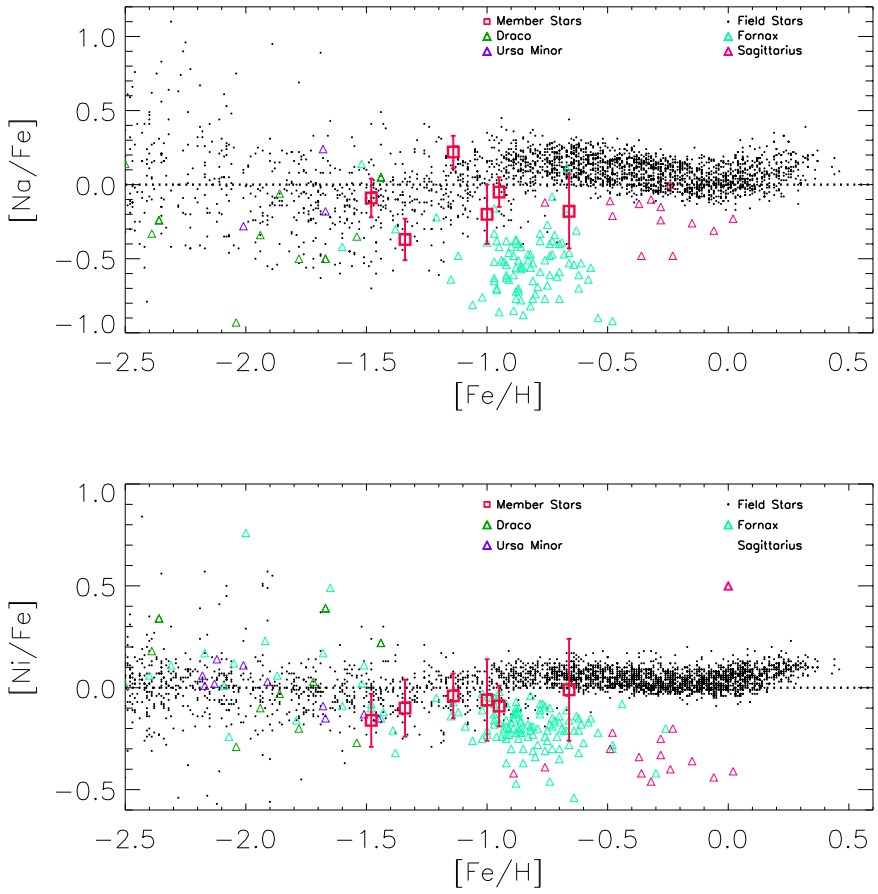

Figure 7. Top: [Na/Fe] vs. [Fe/H]. Bottom: [Ni/Fe] vs. [Fe/H]. The meanings of the symbols are the same as those in Figure 6.

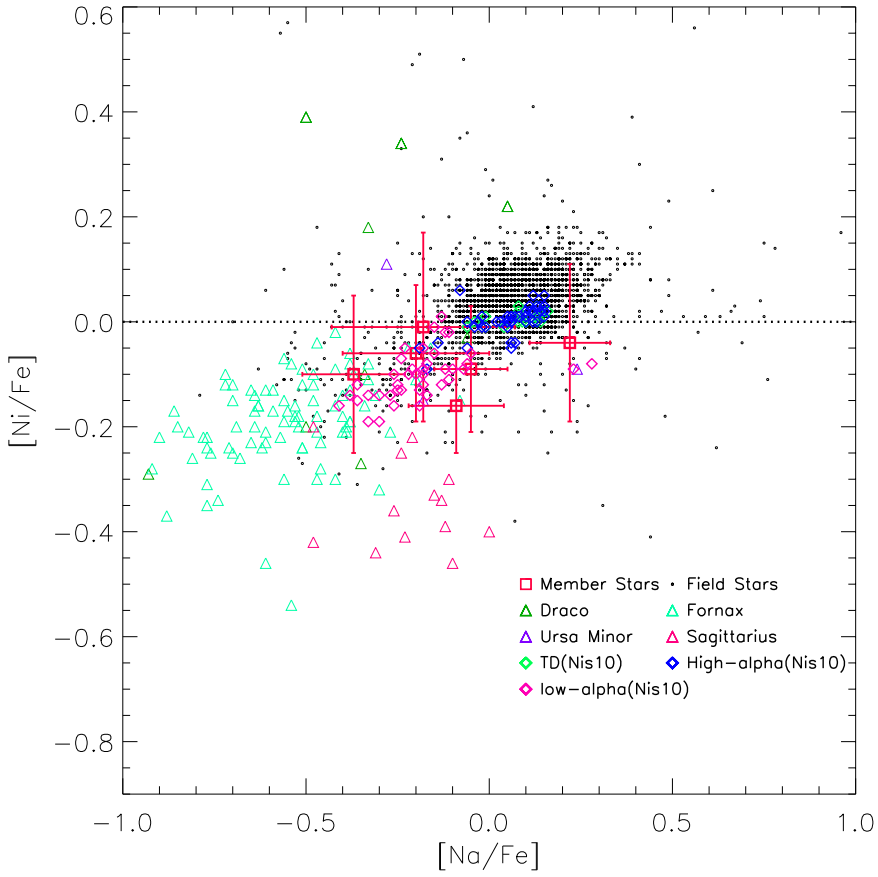

Figure 8. [Na/Fe] vs. [Ni/Fe]. The meanings of the symbols are the same as those in Figure 6.

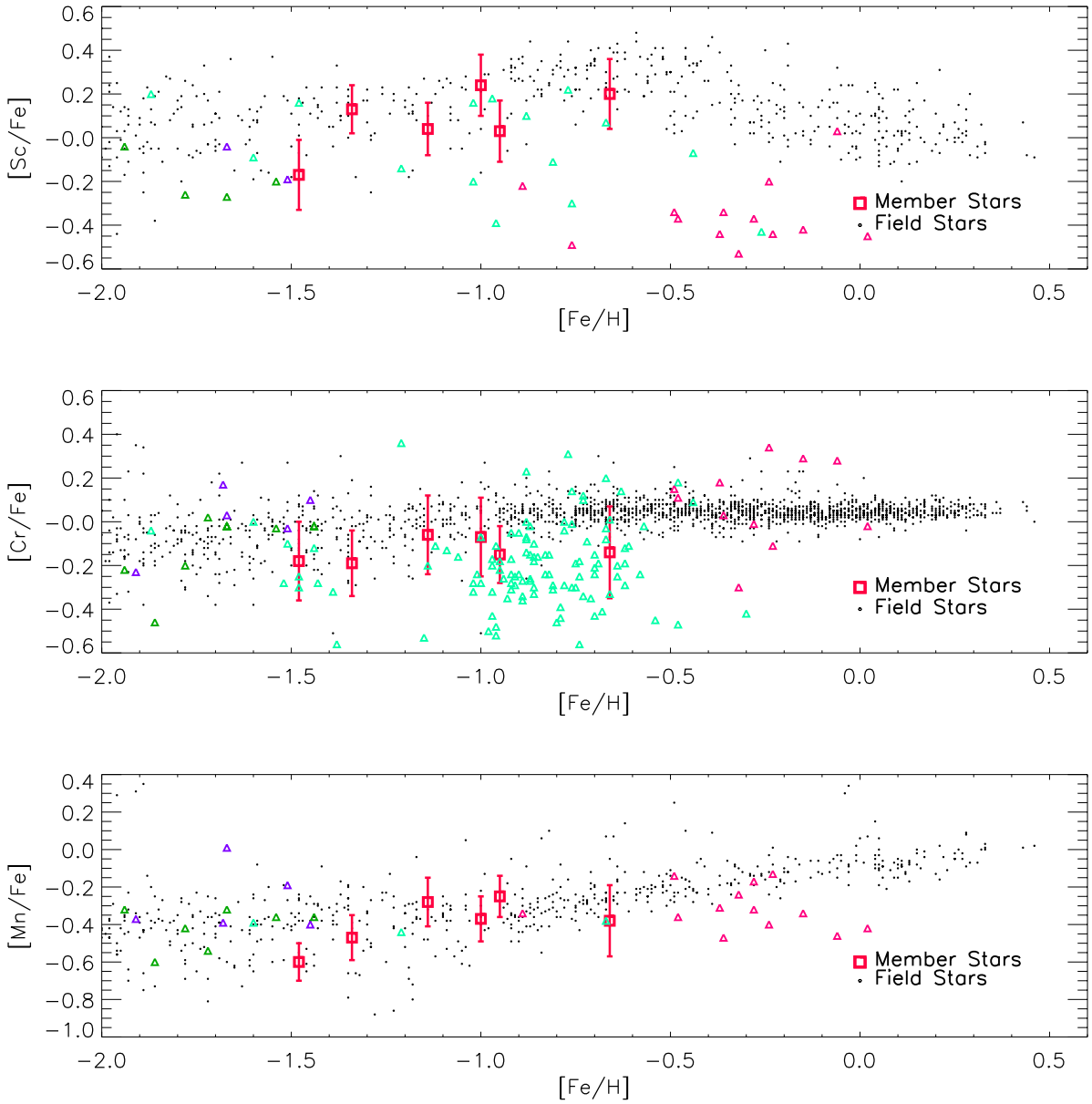

Figure 9. Top: [Sc/Fe] vs. [Fe/H], middle: [Cr/Fe] vs. [Fe/H], and bottom: [Mn/Fe] vs. [Fe/H]. The meanings of the symbols are the same as those in Figure 6.

non-axisymmetric gravitational potentials such as bars and spiral arms. These are usually called kinematic streams and they may have a diverse abundance pattern. In view of this, chemical properties will assist in understanding the origin of LAMOST-N1.

The [α/Fe] ratio is a fundamental chemical signature in stars because it depends on the relative contributions of SN II to SN Ia products that were available when the star was formed. As found in previous studies, the [α/Fe] ratios of most stars in the dSph galaxies are generally lower than Galactic stars with similar metallicity. The average of [α/Fe] of the member stars in LAMOST-N1 is similar with that of the low-α halo populations and separates well from the thick-disk population and high-α halo populations from Nissen & Schuster (2010), which supports the hypothesis that LAMOST-N1 has its origin from stellar systems formed outside of the Milky Way. However, the [α/Fe] of LAMOST-N1 is higher than most of known dSphs, indicating that the progenitor of this stream has a different SFH than with those of dSphs.

Except for one Na-rich star, five member stars with sub-solar Na and Ni values show a similar distribution with the low-α halo populations, indicating that they might have the same origin. These five stars display no clear relation between [Na/Fe] and [Ni/Fe], which is something like the trend with dSphs. One possible explanation would be that [Ni/Fe] and [Na/Fe] in dSph stars are shifted to lower values due to the additional Type Ia SNe production of Fe. Thus, the Na and Ni abundance pattern of member stars supports the extragalactic origin of LAMOST-N1.

The average [Ba/Y] in LAMOST-N1 is about 0.20 dex, which is higher than Galactic stars but lower than stars in known dSphs. Nissen & Schuster (2011) found a trend that high- and low-α stars show well-defined trends of [Ba/Y] with increasing separation as a function of increasing [Fe/H] and that the [Ba/Y] is higher for low-α stars, especially for stars with [Fe/H] > -1.4, which is similar with the pattern of LAMOST-N1. The increasing trend of [Ba/Y] in

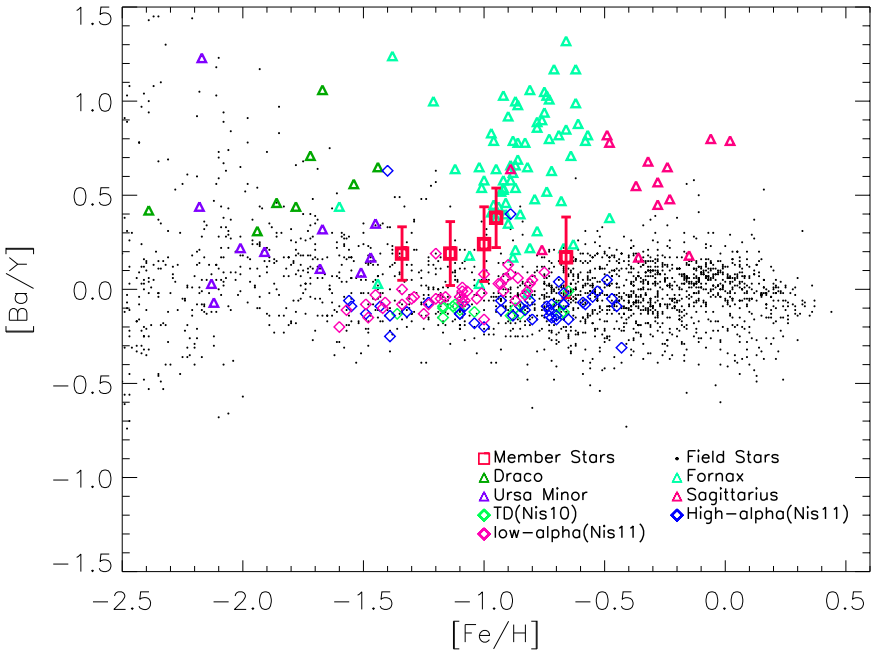

Figure 10. [Ba/Y] vs. [Fe/H]. The meanings of the symbols are the same as those in Figure 6.

LAMOST-N1 may be due to the delayed production of s-process elements by a metal-deficient AGB star. Thus, LAMOST-N1 has a different [Ba/Y] abundance pattern than that of the Galaxy, which suggests that LAMOST-N1 might be a remnant of a dSph.

To summarize, the abundance pattern for [α/Fe] elements [Na/Fe], [Ni/Fe], and [Ba/Y] is very similar to those of LAMOST-N1 and the low-α halo population in Nissen & Schuster (2010) and Nissen & Schuster (2011). The low-α stars, on the other hand, most likely originate from systems with a slower chemical evolution, characterized by additional enrichment from Type Ia supernovae and low-mass AGB stars.

6. Conclusion

We provide the chemical properties of six member stars of the halo stream LAMOST-N1, which were detected as overdensity in dynamical space. These stars exhibits halo-like kinematics with little rotation. With the high-resolution spectra, 11 elemental abundances are determined for the six stars. Detailed abundance distributions are analyzed for α elements, odd-Z elements, Fe-peak elements, and neutron-capture elements. Except for [Na/Fe], other [X/Fe] estimates have very small scatter.

The abundance distributions of [α/Fe] versus [Fe/H], [Na/Fe] versus [Ni/Fe], and [Ba/Y] versus [Fe/H] of LAMOST-N1 are very similar to low-α halo stars of Nissen & Schuster (2010) and [Ba/Y] is higher than Galactic field stars. However, compared with the abundance pattern of dSphs, six member stars show higher [α/Fe] ratios, and lower [Ba/Y] and [Na/Fe]. From the chemistry and kinematics of these six stars, we surmise the LAMOST-N1 might be an accreted population of halo stars, formed in conditions similar to those in early dwarf galaxy satellites. The progenitor of LAMOST-N1 might originate from systems with a slower chemical evolution, characterized by additional enrichment from Type Ia supernovae and low-mass AGB stars.

Many thanks for the constructive comments and suggestions of the anonymous reviewer. This work is supported by the Astronomical Big Data Joint Research Center, cofounded by the National Astronomical Observatories, Chinese Academy of Sciences and the Alibaba Cloud, the National Natural Science Foundation of China under grant No. 11390371, 11573035, 11625313, and the National Key Basic Research Program of China (973 program) 2014CB845701/03. Support from the US National Science Foundation (AST-1358787) to Embry-Riddle Aeronautical University is acknowledged. Guoshoujing Telescope (LAMOST) is a National Major Scientific Project built by the Chinese Academy of Sciences. Funding for the project has been provided by the National Development and Reform Commission. LAMOST is operated and managed by the National Astronomical Observatories, Chinese Academy of Sciences.

ORCID iDs

J. K. Zhao https://orcid.org/0000-0003-2868-8276
W. Aoki https://orcid.org/0000-0002-8975-6829
T. Matsuno https://orcid.org/0000-0002-8077-4617

References

Aoki, W., Beers, T., Lee, Y. S., et al. 2013, AJ, 145, 13
Aoki, W., Honda, S., Beers, T., et al. 2005, ApJ, 632, 611
Asplund, M., Grevesse, N., Sauval, A. J., & Scott, P. 2009, ARA&A, 47, 481
Belokurov, V., Zucker, D. B., Evans, N. W., et al. 2006, ApJL, 642, L137
Bensby, T., Feltzing, S., & Oey, M. S. 2014, A&A, 562, 71
Bergemann, M. 2011, MNRAS, 413, 2184
Bergemann, M., Lind, K., Collet, R., Magic, Z., & Asplund, M. 2012, MNRAS, 427, 27
Casagrande, L., Ramírez, I., Meléndez, J., Bessell, M., & Asplund, M. 2010, A&A, 512, A54
Castelli, F., & Kurucz, R. L. 2003, in IAU Symp. 210, Modelling of Stellar Atmospheres, ed. N. Piskunov, W. W. Weiss, & D. F. Gray (Cambridge: Cambridge Univ. Press), A20
Chambers, K. C., Magnier, E. A., Metcalfe, N., et al. 2016, arXiv:1612.05560
Chiba, M., & Beers, T. C. 2000, AJ, 119, 2843
Cui, X., Zhao, Y., Chu, Y., et al. 2012, RAA, 12, 1197
Dettbarn, C., Fuchs, B., Flynn, C., & Williams, M. 2007, A&A, 474, 857

Grillmair, C. J., & Dionatos, O. 2006, ApJL, 643, L17
Helmi, A., Navarro, J. F., Nordström, B., et al. 2006, MNRAS, 365, 1309
Helmi, A., & White, S. D. M. 1999, MNRAS, 307, 495
Helmi, A., White, S. D. M., de Zeeuw, P. T., & Zhao, H. 1999, Natur, 402, 53
Huang, Y., Liu, X. W., Yuan, H. B., et al. 2015, MNRAS, 454, 2863
Ibata, R., Gilmore, G., & Irwin, M. 1994, Natur, 370, 194
Ishigaki, M. N., Aoki, W., Arimoto, N., & Okamoto, S. 2014, A&A, 562, 146
Ishigaki, M. N., Aoki, W., & Chiba, M. 2013, ApJ, 771, 67
Ishigaki, M. N., Chiba, M., & Aoki, W. 2012, ApJ, 753, 64
Kepley, A. A., Morrison, H. L., Helmi, A., et al. 2007, AJ, 134, 1579
Klement, R., Fuchs, B., & Rix, H. W. 2008, ApJ, 685, 261
Klement, R., Rix, H.-W., Flynn, C., et al. 2009, ApJ, 698, 865
Letarte, B., Hill, V., Tolstoy, E., et al. 2010, A&A, 523, 17
Li, H. N., Zhao, G., Christlieb, N., et al. 2015, ApJ, 110, 13
Liang, X. L., Zhao, J. K., Zhao, G., et al. 2018, ApJ, 863, 4, (Paper I)
Lind, K., Bergemann, M., & Asplund, M. 2012, MNRAS, 427, 50
Liu, C., Feltzing, S., & Ruchti, G. 2015, A&A, 580, A111
Luo, A. L., Zhao, Y. H., Zhao, G., et al. 2015, RAA, 15, 1095
Majewski, S. R., Skrutskie, M. F., Weinberg, M. D., & Ostheimer, J. C. 2003, ApJ, 599, 1082
Martínez-Delgado, D., DOnghia, E., Chonis, T. S., et al. 2015, AJ, 150, 116
McWilliam, A. 1998, AJ, 115, 1640
Monaco, L., Bellazzini, M., Bonifacio, P., et al. 2005, A&A, 441, 141
Navarrete, C., Chanamê, J., Ramírez, I., et al. 2015, ApJ, 808, 103
Nissen, P., & Schuster, W. J. 1997, A&A, 326, 751
Nissen, P., & Schuster, W. J. 2010, A&A, 511, L10
Nissen, P., & Schuster, W. J. 2011, A&A, 530, 15
Nordström, B., Mayor, M., Andersen, J., et al. 2004, A&A, 418, 989
Odenkirchen, M., Grebel, E. K., Rockosi, C. M., et al. 2001, ApJL, 548, L165
Reddy, B. E., Lambert, D. L., & Allende Prieto, C. 2006, MNRAS, 367, 1329
Roederer, I. U., Sneden, C., Thompson, I. B., Preston, G. W., & Shectman, S. A. 2010, ApJ, 711, 573
Schlegel, D., Finkbeiner, D., & Davis, M. 1998, ApJ, 500, 525
Sitnova, T., Zhao, G., Mashonkina, L., et al. 2015, ApJ, 808, 148
Skrutskie, M. F., Cutri, R. M., Stiening, R., et al. 2006, AJ, 131, 1163
Steinmetz, M., Zwitter, T., Siebert, A., et al. 2006, AJ, 132, 1645
Suda, T., Katsuda, Y., Yamada, S., et al. 2008, PASJ, 60, 1159
Venn, K. A., Irwin, M., Shetrone, M. D., et al. 2004, AJ, 128, 1177
Wylie-de Boer, E., Freeman, K., & Williams, M. 2010, AJ, 139, 636
Xing, Q. F., & Zhao, G. 2014, ApJ, 790, 33
York, D. G., Adelman, J., Anderson, J. E., et al. 2000, AJ, 120, 1579
Zhao, C., & Newberg, H. J. 2006, arXiv:astro-ph/0612034
Zhao, G., Zhao, Y. H., Chu, Y. Q., et al. 2012, RAA, 12, 723
Zhao, J., Zhao, G., Chen, Y., et al. 2014, ApJ, 787, 31
Zhao, J., Zhao, G., Chen, Y., et al. 2015, RAA, 15, 1378
Zhao, J. K., Zhao, G., & Chen, Y. Q. 2007, PNAOC, 4, 153